



Alabama State University
Boston University
Bryn Mawr College
New Jersey Institute of Technology
University of Pennsylvania
University of Texas at Austin
Washington University in St. Louis

End of Summer REU Symposium

Thursday, August 4, 2022, 10:00 am – 12:00 pm (CST)

In Person: Whitaker Hall, Room 100

or Virtual: [Zoom Link](#) (Meeting ID 972 7690 6842)

10:00 am - 10:15 – Welcoming Remarks

Guy Genin, PhD, CEMB Co-Director and

Patricia Widder, CEMB Education Program Coordinator and Senior Lecturer in Biomedical Engineering

10:15 am - 10:30 am – Melanie Roberts, St. Olaf College

Jessica Wagenseil Lab

Limited Effect of In Vivo Pressure, Axial Stretch, and Viscosity in Mass Transport of Murine Ascending Aorta

[Abstract](#) | [Poster](#)

10:35 am - 10:50 am – Ari Rapalino, Washington University in St. Louis

Nathaniel Huebsch Lab

Cell Stretcher for Studying the Effects of Mechanical Stress on Cardiomyocytes

[Abstract](#) | [Poster](#)

10:55 am - 11:10 am – Kenny Nguyen, Louisiana State University

Amit Pathak Lab

Role of Extracellular Matrix Proteins on Collective Cell Migration

[Abstract](#) | [Poster](#)

11:10 - 11:20 – Break

11:20 am - 11:35 am – Kenadie Doty, Buena Vista University

Marcus Foston Lab

Ultraviolet Initiated Crosslinking in TEMPO and Benzophenone Cellulose Nanocrystal Based Films

[Abstract](#) | [Poster](#)

11:40 am - 11:55 am – Siena Smith, University of Michigan - Dearborn

Gretchen Meyer Lab

Follistatin is Required for Mass Maintenance But Not Force Recovery Following Muscle Stimulation

[Abstract](#) | [Poster](#)

12:00 - 12:15 – Closing Remarks

Guy Genin, PhD, CEMB Co-Director

Patricia Widder, CEMB Education Program Coordinator

Lunch and beverages will be available afterwards in Brauer Hall, 2nd Floor Lounge.

Pressure, Axial Stretch and Viscosity Have No Effect on Hydraulic Conductance in Mouse Ascending

Aorta Melanie G. Roberts^{1,2,*}, Christie L. Crandall², Jacob P. Rother² and Jessica E. Wagenseil²
St. Olaf College¹ and Washington University, St. Louis, MO²

Introduction: Replicating physiological conditions is important when measuring hydraulic conductance (L_p) of healthy and diseased tissue. Previously, we found an effect of fragmented elastin on arterial L_p in mouse models of human disease. Previous experiments were done at 100 mmHg, 1.1x axial stretch, and with phosphate buffered saline (PBS) as the solvent. In vivo, pressure and axial stretch ratio vary in the ascending thoracic aorta (ATA), and blood viscosity is higher than PBS. The goal of this study was to determine if these in vivo conditions affect L_p in the mouse ATA.

Materials and Methods: Twenty-six 3-4 month-old male C57BL6/J mice were euthanized by carbon dioxide inhalation in compliance with the Institutional Animal Care and Use Committee. ATAs were dissected and cannulated on a pressure myograph. Baseline experimental conditions included stretching the ATA to 1.1x axial stretch and inflating to 100 mmHg (ΔP) with a static fluid column of PBS. The endothelial cell layer was stripped by running an air bubble through the lumen to measure only L_p through the medial and adventitial layers of the wall. Loaded length and outer diameter were recorded. A bubble was added to the fluid tubing and monitored for 30-60 min to calculate fluid flux (J_v). Without a concentration gradient, hydraulic conductance (L_p) can be calculated by $L_p = J_v/\Delta P$. There were three varied experimental conditions: pressure, axial stretch, and viscosity. For pressure, N=4-5 ATAs were exposed to 80 and 120, 90 and 140, or 100 mmHg with PBS, and L_p was determined at 1.1x axial stretch. For axial stretch, each ATA was pressurized to 100 mmHg with PBS and N=4 ATAs were axially stretched to 1.1x, 1.2x, 1.3x, 1.4x, and 1.5x for L_p measurements. N=3 ATAs failed at a 1.5x stretch ratio and were not included in the analyses. For viscosity, L_p for N=5 ATAs was first measured with PBS (~1 cP) at 100 mmHg and 1.1x axial stretch. The fluid in the pressure column and bath were then replaced with a 1.4 mg alginate/1 mL PBS (~3.5 cP) solution. The ATA was allowed to equilibrate for 15 minutes and L_p was measured again.

Results and Discussion: There are no significant changes in L_p of mouse ATAs as an effect of differing pressures and axial stretch ratios (by one-way ANOVA), or solvent viscosity (by t-test) (Fig. 1). The results for the pressure experiment (Fig. 1A, performed first and by multiple individuals) are more variable and have slightly higher L_p values than the axial stretch (Fig. 1B) and viscosity (Fig. 1C) experiments, indicating that experimenter experience may influence the measured L_p values. The alginate data in the viscosity experiment is less variable than the PBS data (Fig. 1C), indicating that a thicker, more viscous fluid may reduce variability of the L_p measurements but has no effect on the absolute values.

Conclusions: Previous L_p experiments in our lab maintained a constant pressure of 100 mmHg, 1.1x axial stretch ratio, and used PBS as the fluid solvent (viscosity ~1cP). The results here demonstrate these past experimental conditions as valid comparisons to in vivo conditions with variable pressure, axial stretch, and blood as the solvent (viscosity ~3.5 cP). Other studies also found that L_p is independent of pressure and viscosity in rat and rabbit arteries. However, the pressure and viscosity dependence of L_p in the mouse ATA was previously unknown and this is the first reported data on the dependence of L_p on axial stretch ratio, to our knowledge. The results confirm the validity of previous experimental procedures. Future work will determine L_p in mouse models of aortic disease to determine how mass transport changes may contribute to pathogenesis.

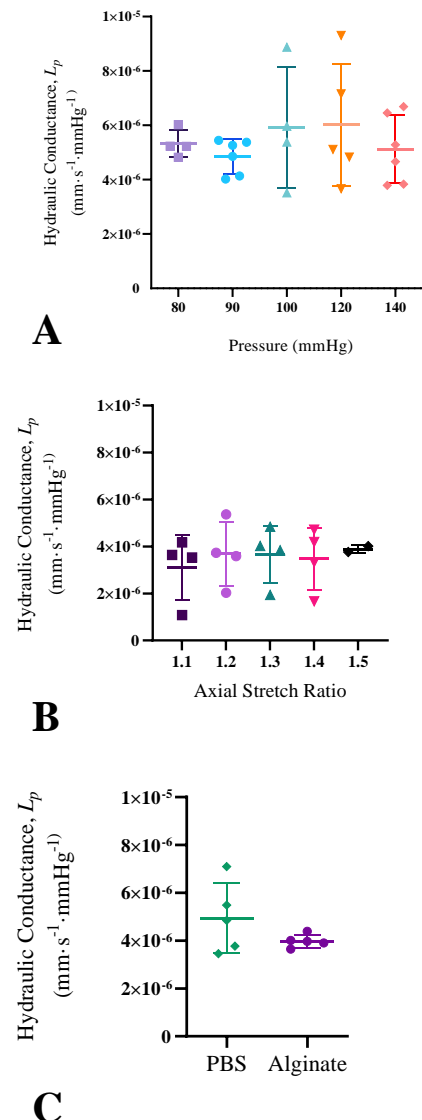


Figure 1: Hydraulic conductance at differing pressures (A), stretch ratios (B) and solvent viscosities (C).

Introduction

Replicating physiological conditions is important when measuring hydraulic conductance of healthy and diseased tissue. Previously, our lab has found an effect of fragmented elastin on the hydraulic conductance of mouse arteries.³ Many of the experimental conditions were controlled, but in vivo, pressure and axial stretch ratio vary in the ascending thoracic aorta (ATA), and viscosity of the blood is different from our experimental solvent: phosphate buffered solution (PBS)⁶. The goal of this study was to determine if these in vivo conditions affect hydraulic conductance (L_p) in the ATA.

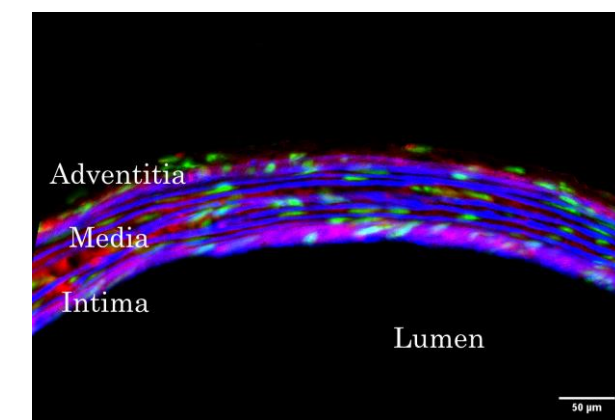


Fig 1: Cross-sectional image showing the three layers of the aorta with cell nuclei in green, elastic lamellae in blue and collagen fibers in red.

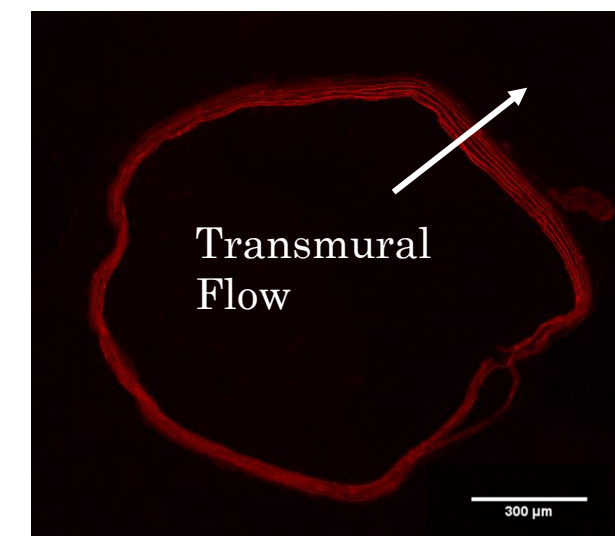
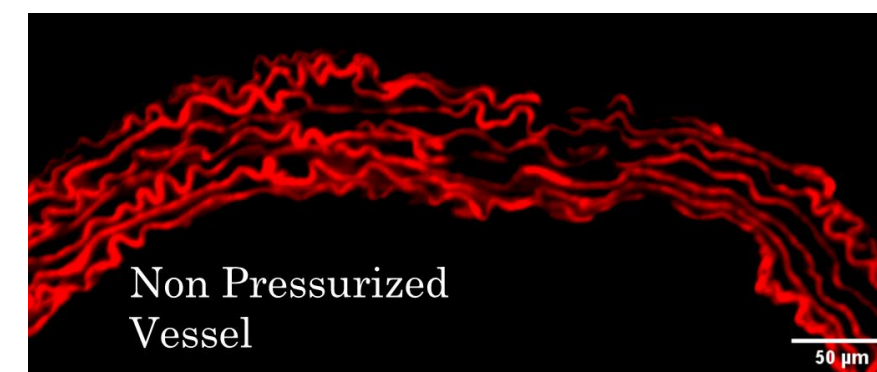


Fig 2: Cross-sectional image showing the direction of transmural fluid flow.

Results



As the ATA is pressurized, the elastic lamellae begin to straighten and the fenestrae (not pictured) change shape.

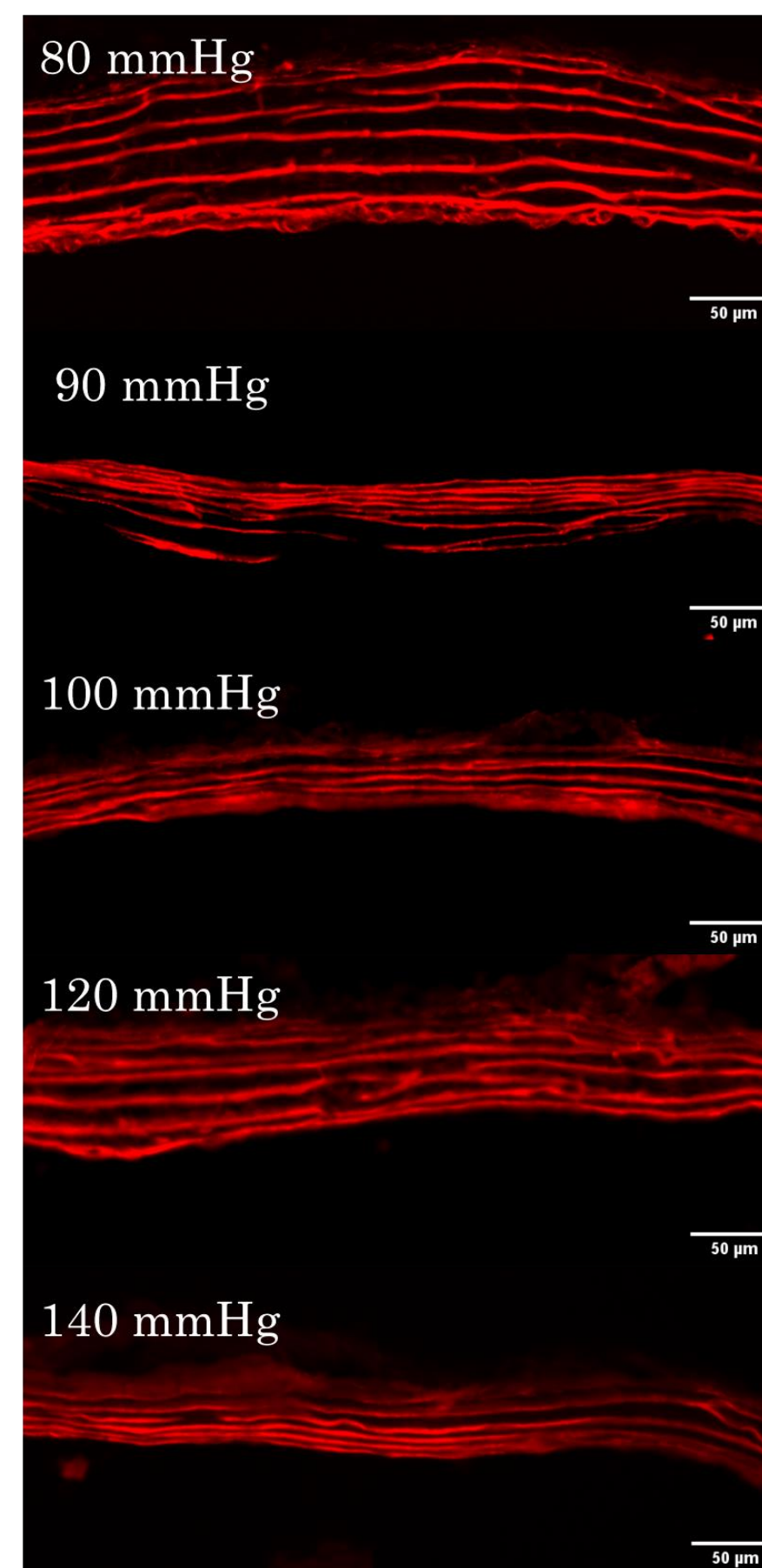


Fig 6: Elastic lamellae are shown at five different pressures and compared to a non-pressurized vessel.

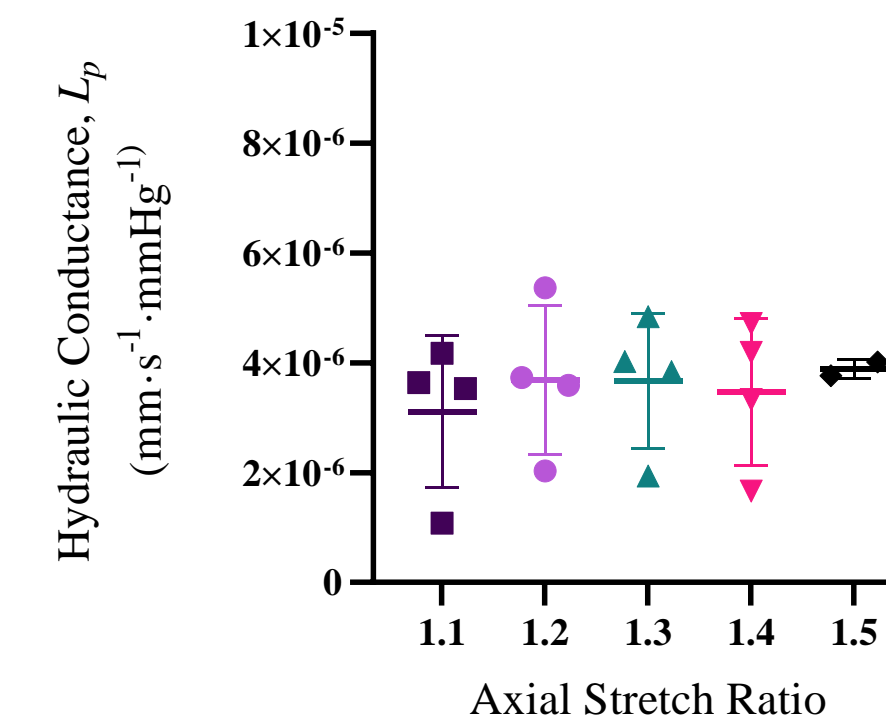


Fig 4: Measured values for hydraulic conductance at differing axial stretch ratios.

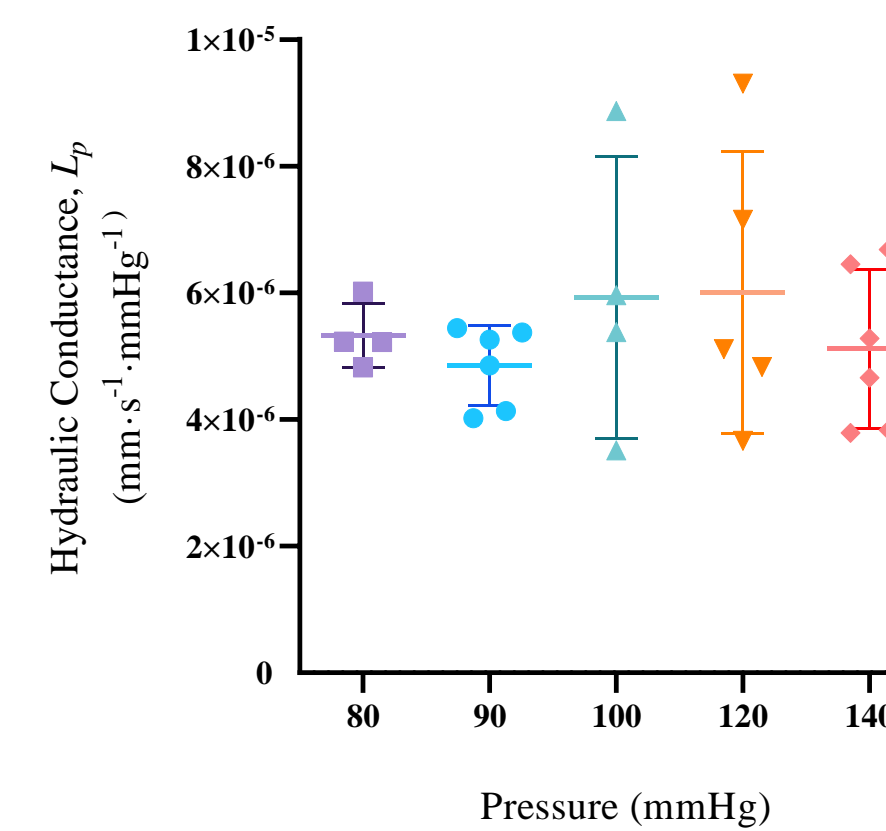


Fig 5: Measured values for hydraulic conductance at differing pressures representing normal blood pressure (120/80 mmHg), control (100 mmHg) and hypertension (140/90 mmHg).

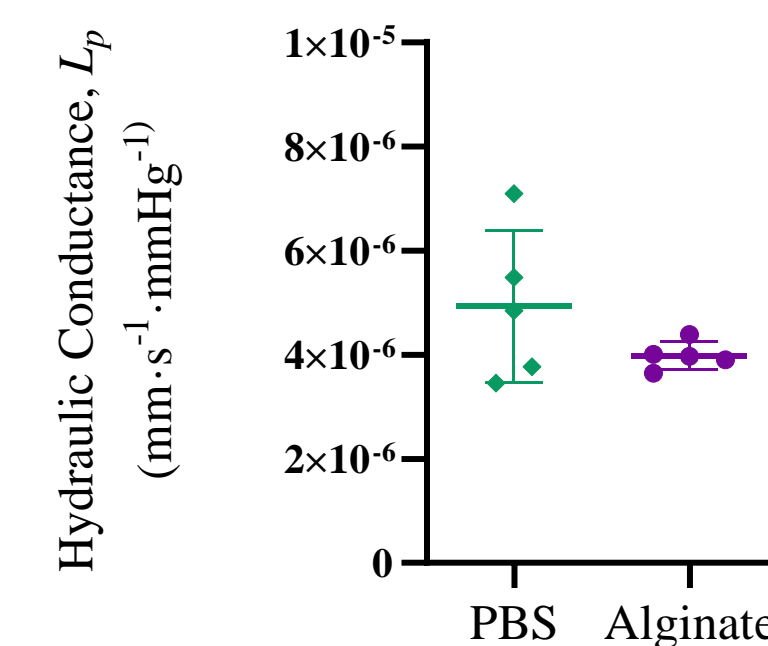


Fig 7: Measured values for hydraulic conductance using solvents of differing viscosity (PBS (~1cP) and alginate (~3.5cP)).

Impact

- There were no significant changes in the hydraulic conductance of mouse ATA as an effect of differing pressures and axial stretch ratio (by one-way ANOVA), or solvent viscosity (by T-test).
- Result demonstrate past experimental conditions are valid comparisons to in vivo conditions.
- Other studies also found that L_p is independent of pressure and viscosity in rat⁷ and rabbit⁸ arteries.
 - However, pressure and viscosity dependence of L_p in the mouse ATA was previously unknown.
- This is the first reported data on the dependence of L_p on axial stretch ratio, to our knowledge.

Next Steps

The results confirm the validity of previous experimental procedures. Future work will determine L_p in mouse models of aortic disease to determine how mass transport changes may contribute to pathogenesis.

References

- Baldwin, A. L., Wilson, L. M., & Simon, B. R. (1992). Effect of pressure on aortic hydraulic conductance. *Arteriosclerosis and Thrombosis: A Journal of Vascular Biology*, 12(2), 163-171. <https://doi.org/10.1161/01.ATV.12.2.163>
- Choi, K. Y., Comerford, A., Sherwin, S. J., & Weinberg, P. D. (2016). Intimal and medial contributions to the hydraulic resistance of the arterial wall at different pressures: A combined computational and experimental study. *Journal of The Royal Society Interface*, 13(119), 20160234. <https://doi.org/10.1098/rsif.2016.0234>
- Cocciolone, A. J., Johnson, E., Shou, J. Y., & Wagenseil, J. E. (2018). Elastic fiber fragmentation increases transmural hydraulic conductance and solute transport in mouse arteries. *Journal of Biomechanical Engineering*. <https://doi.org/10.1115/1.4042173>
- Gouveia E Melo, R., Silva Duarte, G., Lopes, A., Alves, M., Caldeira, D., Fernandes E Fernandes, R., & Mendes Pedro, L. (2022). Incidence and Prevalence of Thoracic Aortic Aneurysms: A Systematic Review and Meta-analysis of Population-Based Studies. *Seminars in Thoracic and Cardiovascular Surgery*, 34(1), 1-16. <https://doi.org/10.1053/j.semthor.2021.02.029>
- Gao, X., & Kassab, G. S. (2003). Variation of mechanical properties along the length of the aorta in C57bl/6 mice. *American Journal of Physiology-Heart and Circulatory Physiology*, 285(6), H2614-H2622. <https://doi.org/10.1152/ajpheart.00567.2003>
- Nader, E., Skinner, S., Romana, M., Fort, R., Lemonne, N., Guillot, N., Gauthier, A., Antoine-Jonville, S., Renoux, C., Hardy-Dessources, M.-D., Stauffer, E., Joly, P., Bertrand, Y., & Connes, P. (2019). Blood rheology: Key parameters, impact on blood flow, role in sickle cell disease and effects of exercise. *Frontiers in Physiology*, 10. <https://www.frontiersin.org/articles/10.3389/fphys.2019.01329>
- Shou, Y., Jan, K., & Ramschitzki, D. S. (2006). Transport in rat vessel walls. I. Hydraulic conductivities of the aorta, pulmonary artery, and inferior vena cava with intact and denuded endothelia. *American Journal of Physiology-Heart and Circulatory Physiology*, 291(6), H2758-H2771. <https://doi.org/10.1152/ajpheart.00610.2005>
- Tedgui, A., & Lever, M. J. (1984). Filtration through damaged and undamaged rabbit thoracic aorta. *The American Journal of Physiology*, 247(5 Pt 2), H784-791. <https://doi.org/10.1152/ajpheart.1984.247.5.H784>

Fluid Transport Experiment

Experimental Set up

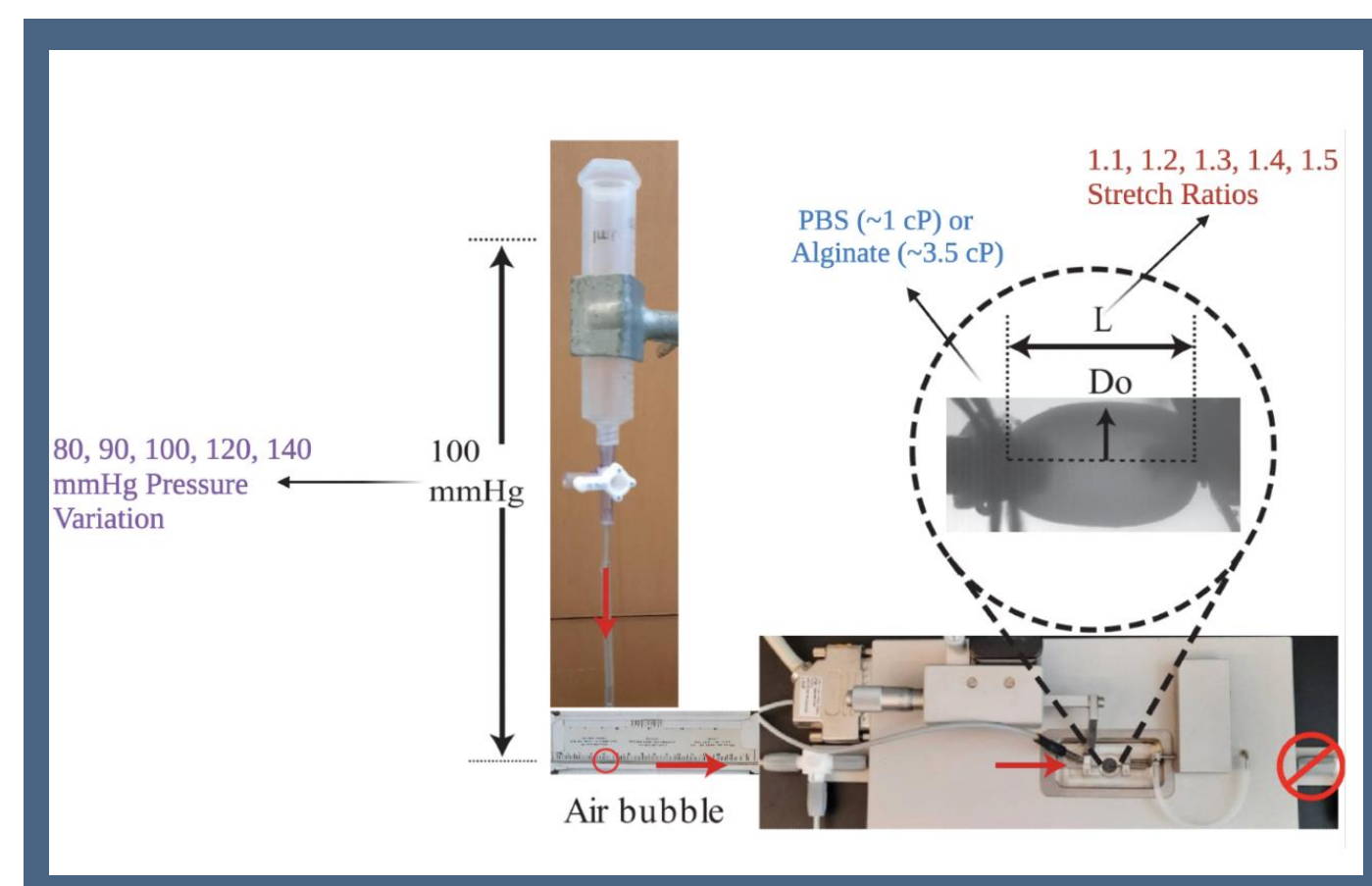
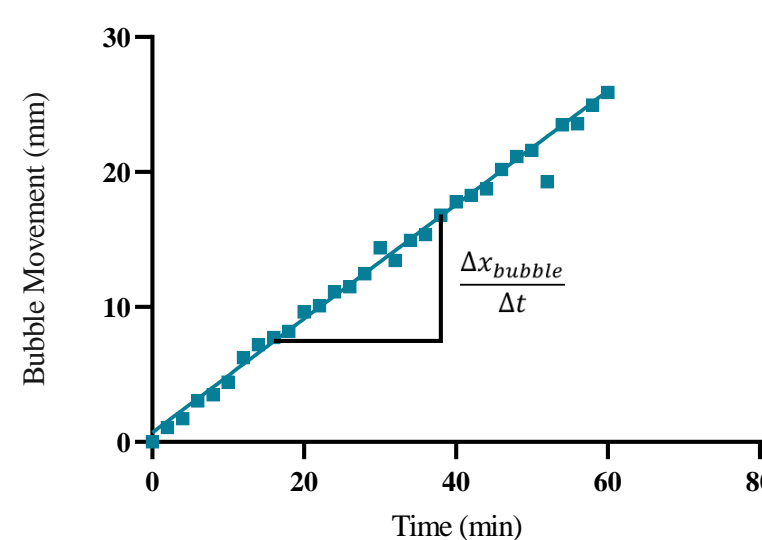


Fig 3: The ATA was cannulated onto a pressure myograph. Intraluminal pressure was maintained with a static pressure column and an air bubble was monitored over time. Different experimental conditions are shown in color.

Mass Transport Theory



$$J_v = \frac{d_T^2 * \frac{\Delta x_{bubble}}{\Delta t}}{4 * d_A * L_A} \quad J_v = L_p \Delta P$$

J_v Solvent flux

L_p Hydraulic conductance

A Low Cost, Customized System For Exogenous Cell Stretch

Authors: Ari Rapalino*, Lavanya Aryan, David Shuftan, Ghiska Rhamadita, Sydney Neal, Nathaniel Huebsch

Introduction: iPSC derived cardiomyocytes are a more and more popular tool for cardiac research and drug development, but their immaturity remains a problem. As the embryonic heart grows, the cardiomyocytes within experience stretch, causing their length to more than double. We aim to simulate iPSC-cardiomyocyte maturation by applying exogenous stretch to cultured cells. However, commercial devices for stretching cultured cells are expensive and often involve proprietary materials, making it challenging to parallelize studies and to understand how those materials interact with cells. To overcome these obstacles, we used 3D-printing based fabrication to create a simple cell stretcher device to apply exogenous tension to cultured cells. Device biocompatibility was demonstrated using C2C12 myoblasts.

Materials and Methods: The finalized cell stretcher design consisted of commercially available vise and a custom made Sylgard 184 based chamber to hold media and cells. The chamber was designed using Autodesk Inventor. First, a 3D print in the shape of the final device was created in FormLabs Clear Resin on a FormLabs 3 stereolithographic printer. PDMS chambers were then created by Hydrogel Assisted Stereolithographic Elastomer prototyping (HASTE; Simmons *et al. BioRxiv*, 2022). Briefly, a negative Agar mold was cast over the 3D print, and a Sylgard 184 Polydimethylsiloxane (PDMS) was then cast off the agar negative. We first screened for the optimal ratio of PDMS crosslinker:base by performing tensile testing on an Instron 5542 tester using specimens with standard ASME testing dimensions. We next tested the actual failure strain of the chamber themselves. Preliminary studies on cell compatibility and cell stretch were performed with C2C12 myoblasts.

Results and Discussion: Final gross cost estimate of the device (Figure 1C) is around \$20, as opposed to existing commercial devices gross cost of \$1051. After the initial chamber and vise design was realized and successfully created using the double molding technique, two types of testing, material and cell viability, were done to ensure the cell stretcher device could perform as needed. First, the chamber modulus was adjusted to achieve an ultimate strain greater than 50% (existing commercial devices failed at 25% strain). Material testing of different PDMS crosslinker:base ratios and subsequent failure testing of actual chambers resulted in the 1:18 ratio giving the greatest ultimate strain of around 0.87 on average (Figure 1A). Location of chamber failure was generally consistent with stress simulation run on Inventor Autodesk (Figure 1B).

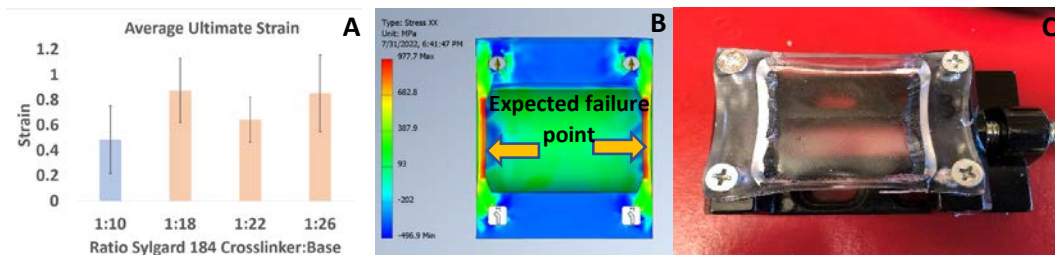


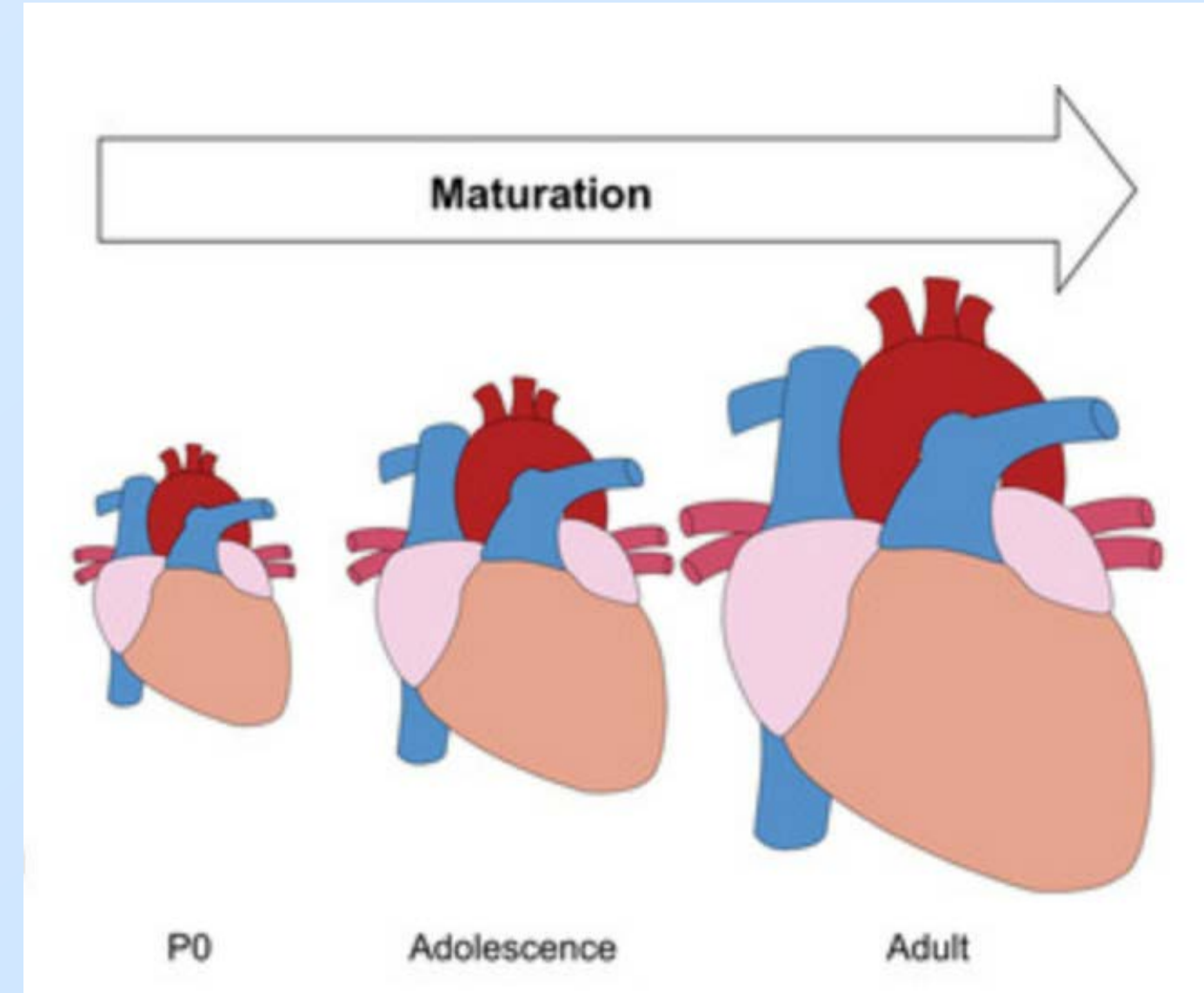
Figure 1. A) shows the average ultimate strain of chambers with highest ultimate strain in material testing after being stretched until failure, with the standard PDMS ratio value in blue, increased ratios in brown. The n value for each was 3, and the error bars represent standard deviation. B) Shows the stress simulation of the chamber on Inventor Autodesk with expected failure point marked. C) Picture of device with chamber at maximum strain.

Next, every seeded chamber, over multiple seedings, displayed recognizable cell growth and proliferation. In addition, said chambers when stretched, demonstrated cell-chamber adherence and recognizable stretch of the cells themselves.

Conclusions: The cell stretcher's eventual purpose is to apply mechanical load to iPSC derived cardiomyocytes, which resemble embryonic cardiomyocytes in terms of maturity, to simulate the developmental changes that are triggered by stretch. The 18:1 PDMS ratio determined from material testing, and the viability and adherence of the myoblasts seeded on the chambers, optimized the functionality of the device. Future studies will include a more sophisticated linear actuation device to better image the chamber while stretched.

Introduction

iPSC derived cardiomyocytes are a more and more popular tool for cardiac research and drug development, but their immaturity remains a problem. As the embryonic heart grows, the cardiomyocytes within experience stretch, causing their length to more than double². We aim to simulate iPSC-cardiomyocyte maturation by applying exogenous stretch to cultured cells. However, commercial devices for stretching cultured cells are expensive and often involve proprietary materials, making it challenging to parallelize studies and to understand how those materials interact with cells. To overcome these obstacles, we used 3D-printing based fabrication to create a simple cell stretcher device to apply exogenous tension to cultured cells. Device biocompatibility was demonstrated using C2C12 myoblasts.



Methods

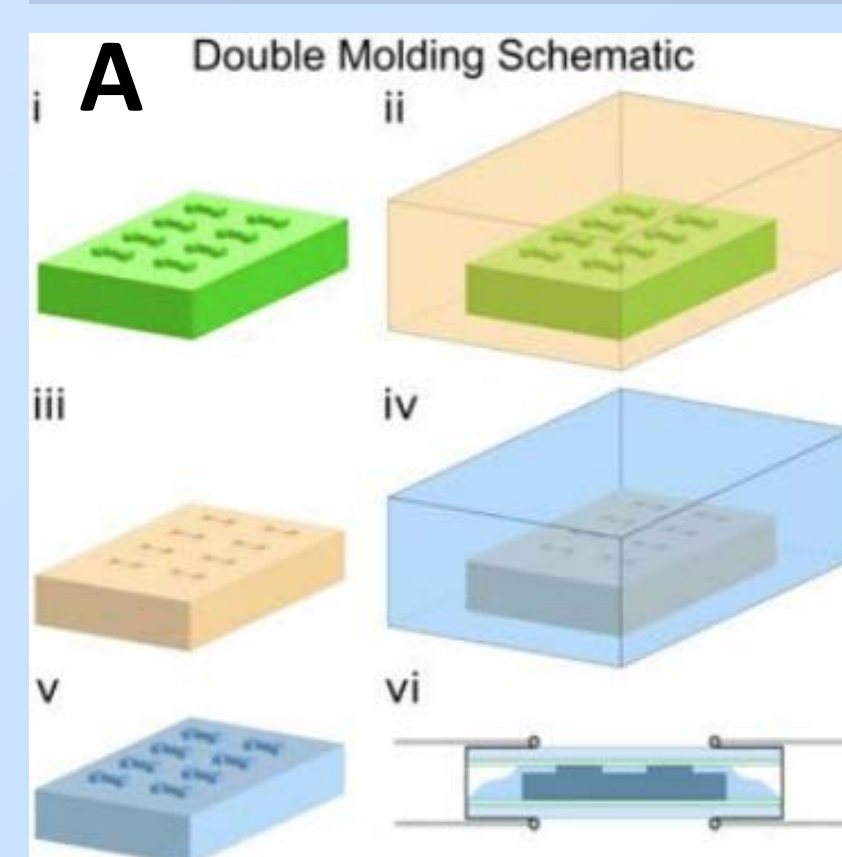
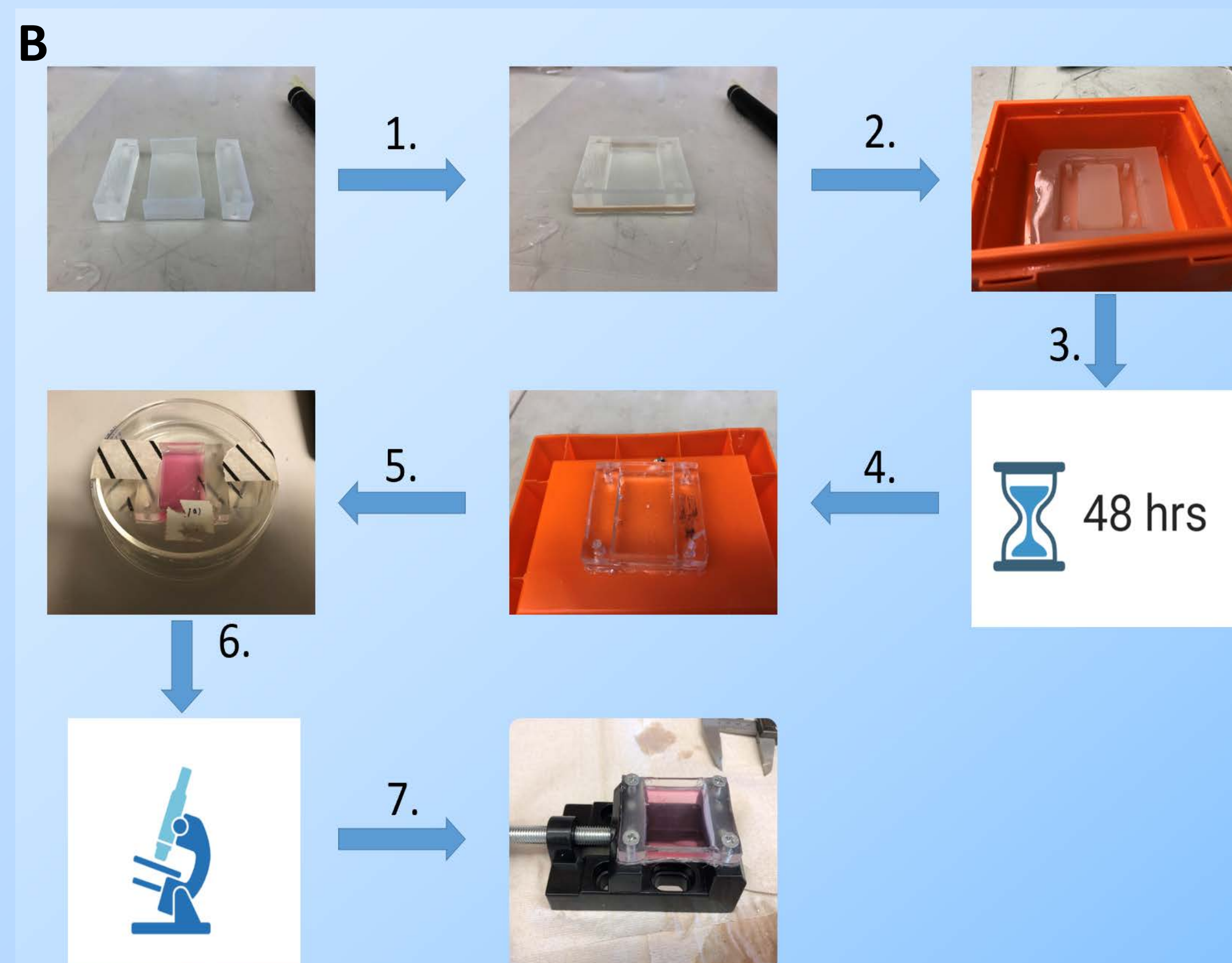


Figure 1. A) Double Molding Schematic developed in Huebsch Lab¹. B) Sylgard 184 PDMS Chamber is made by double molding technique. After PDMS cures for 48 hours, chamber is seeded and imaged. After reaching sufficient confluency, chamber is stretched, fixed, and imaged again.



Material Testing

Material Properties

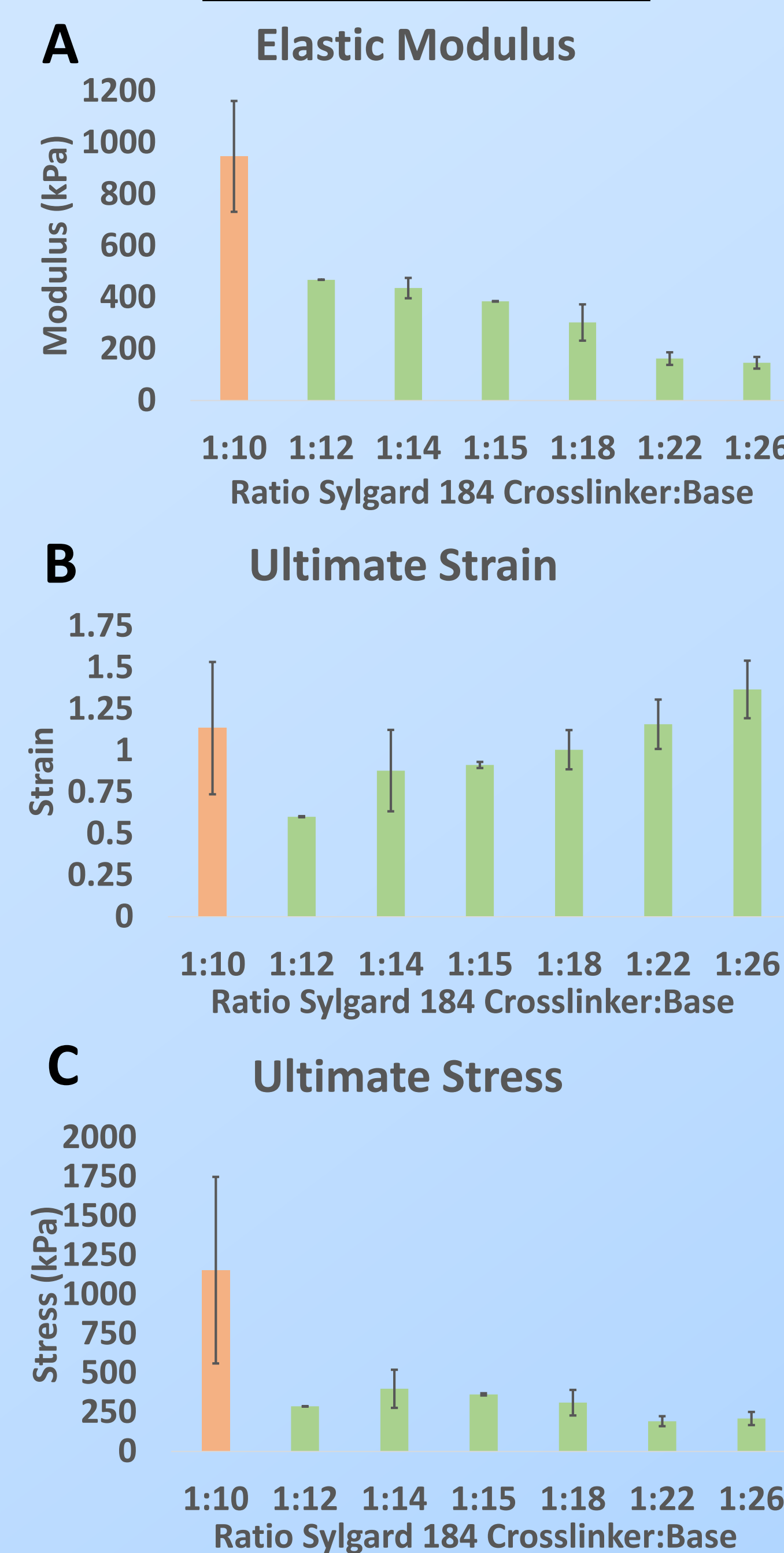


Figure 2. A) above shows the elastic modulus, B) ultimate strain, and C) ultimate stress of the Polydimethylsiloxane at different ratios of crosslinker:base using an Instron 5542 Material Testing device. The 1:10 ratio (in orange) is the standard ratio used.

Chamber Properties

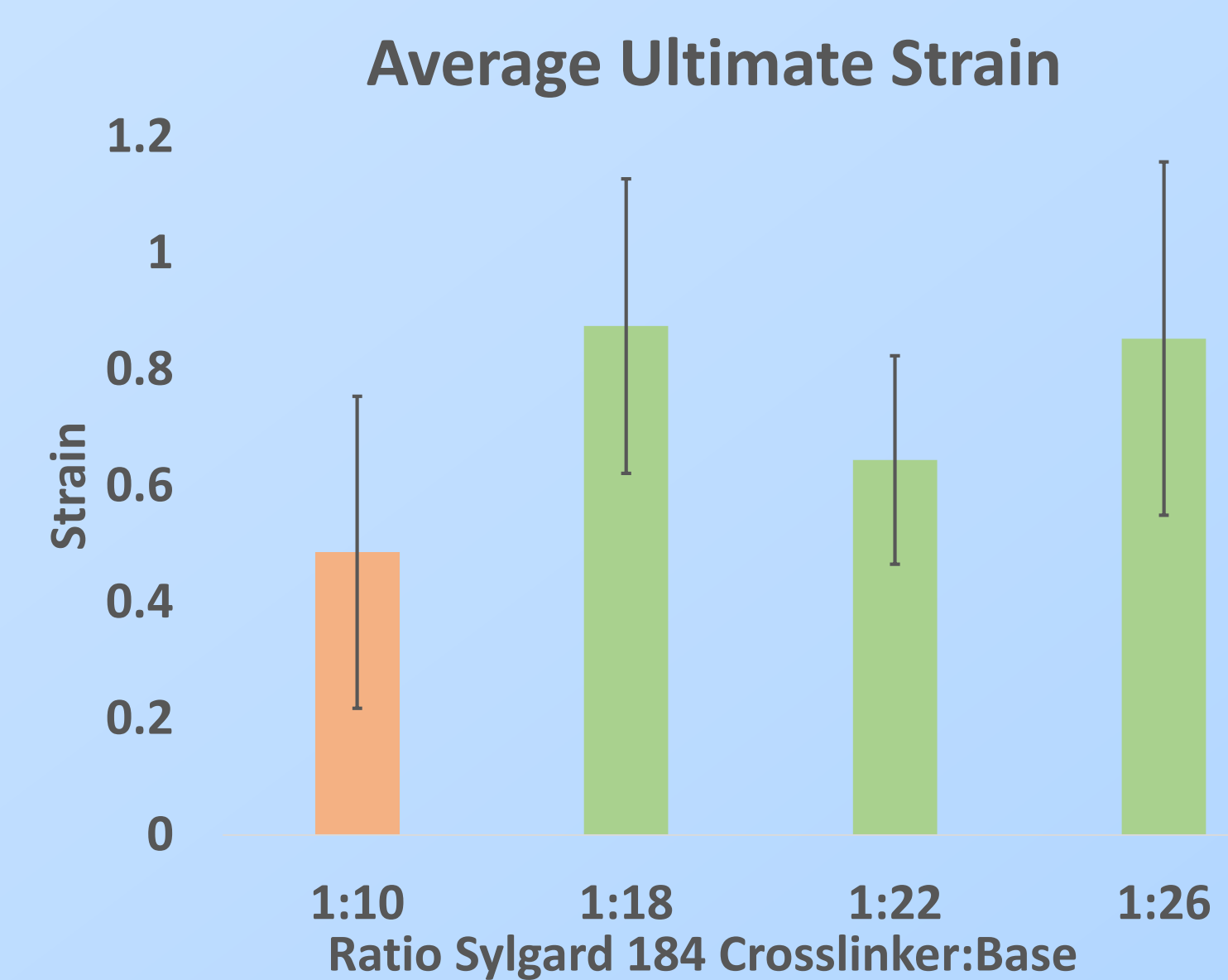


Figure 3. shows the average ultimate strain of the created PDMS chambers of different crosslinker:base ratios. The 1:10 ratio (in orange) is the standard ratio used. From 1-way ANOVA, data is not statistically significant.

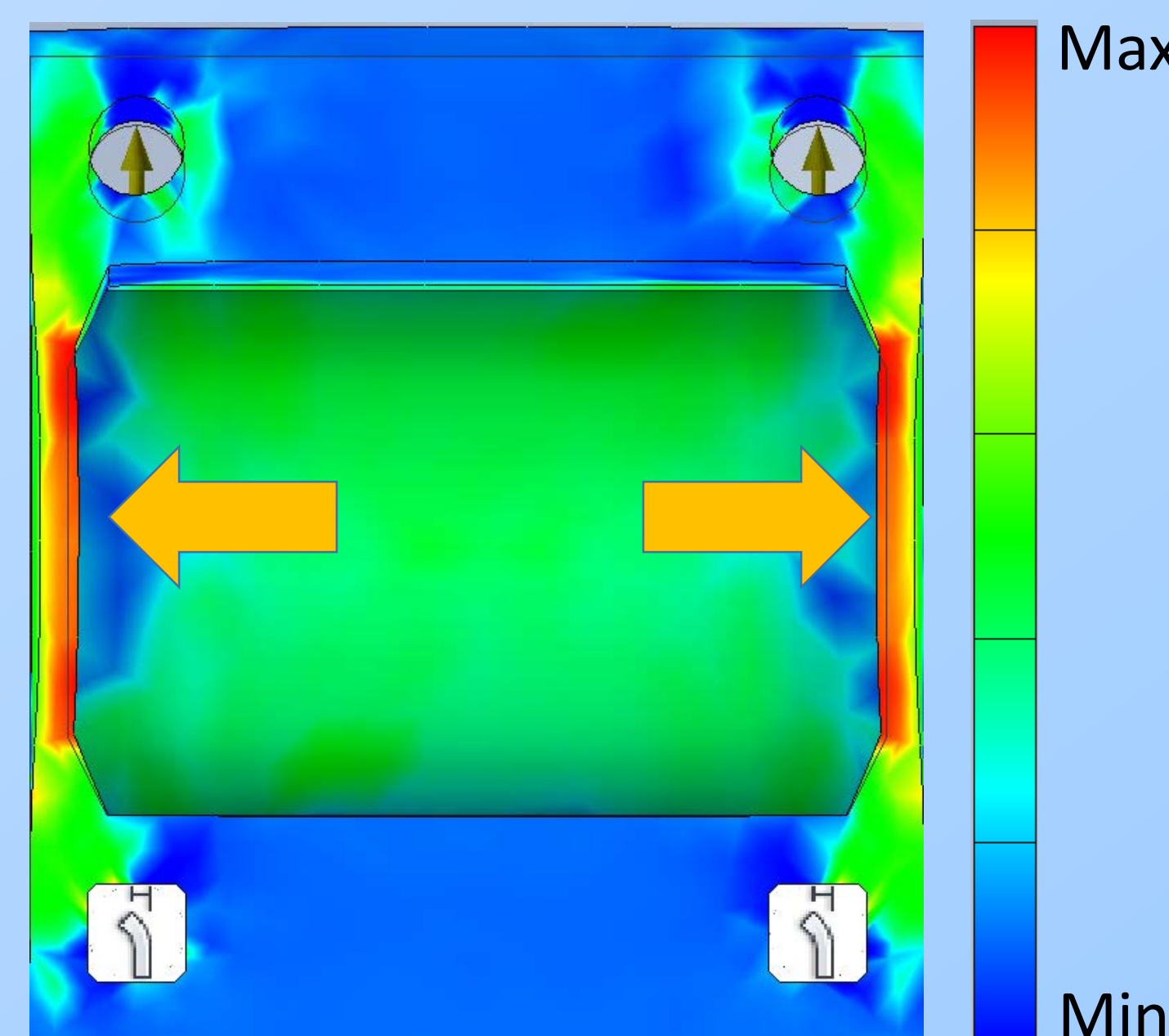


Figure 4. shows a linear stress simulation in the vertical direction from Autodesk Inventor with most likely failure points indicated by yellow arrows and areas of highest stress (red).

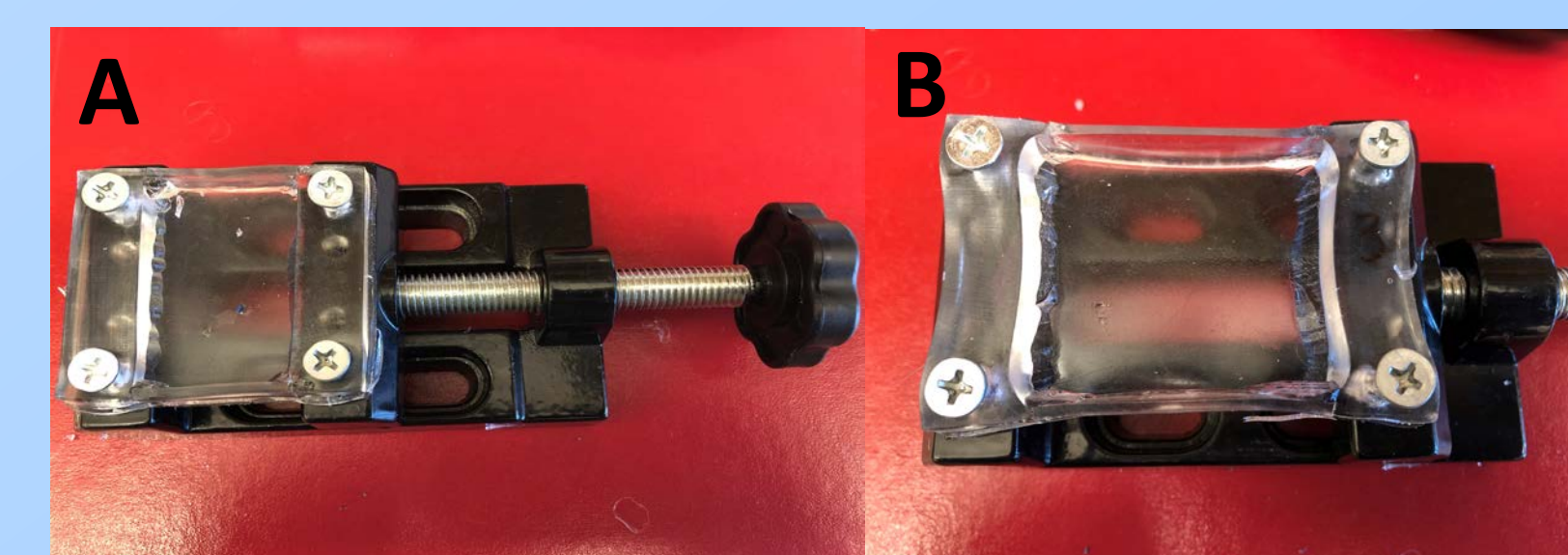
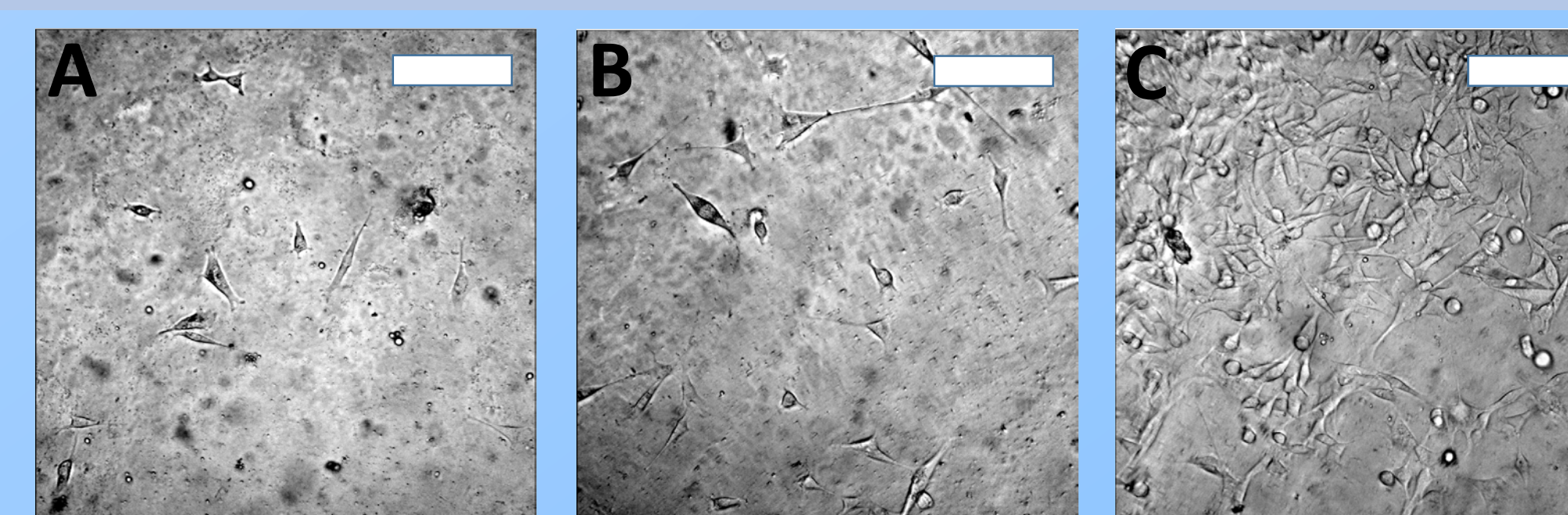


Figure 5. A) image of device before stretch and failure. B) image of device after stretch and before failure C) image of device after stretch and failure. Failure location consistent with simulation

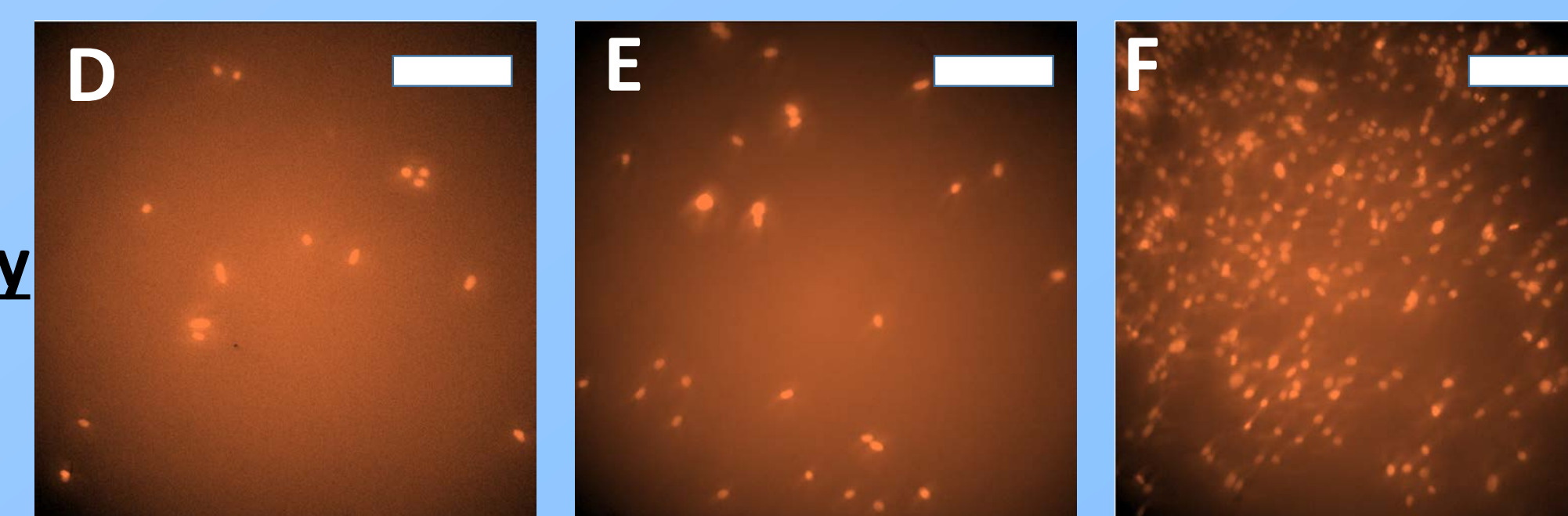
Biocompatibility of device

Figure 6. Images from Nikon of C2C12 myoblasts expressing H2B-mCherry fusion protein seeded on chamber showing growth over 4 days. Scale bars are 250 microns. Images were taken on BF filter after A) 2 days, B) 3 days, C) 4 days and on TRITC filter after D) 2 days, E) 3 days, F) 4 days

Brightfield



H2B-mCherry



Conclusions

- Based on the results on the material testing, the ideal ratio for the base:crosslinker of the PDMS is 18:1. The 18:1 ratio allows for an average ultimate chamber strain of 0.87, which is significantly better than the standard 10:1 ratios average ultimate chamber strain of 0.48.
- The myoblasts seeded on the chambers successfully adhered to the chambers and grew without any hindrance.
- The final cell stretcher device design has an estimated gross cost of 15\$, which is significantly less expensive than the original design (StrexCell) which costs up to \$1051.

Future Work

- Bond stencils used for cardiomyocyte growth and stretch chamber to check for stencil delamination
- Design and build new vise that allows for easier imaging of chambers while still on vise
- Seed cardiomyocytes instead of myoblasts on chambers and image to determine effectiveness on cardiomyocytes.

References

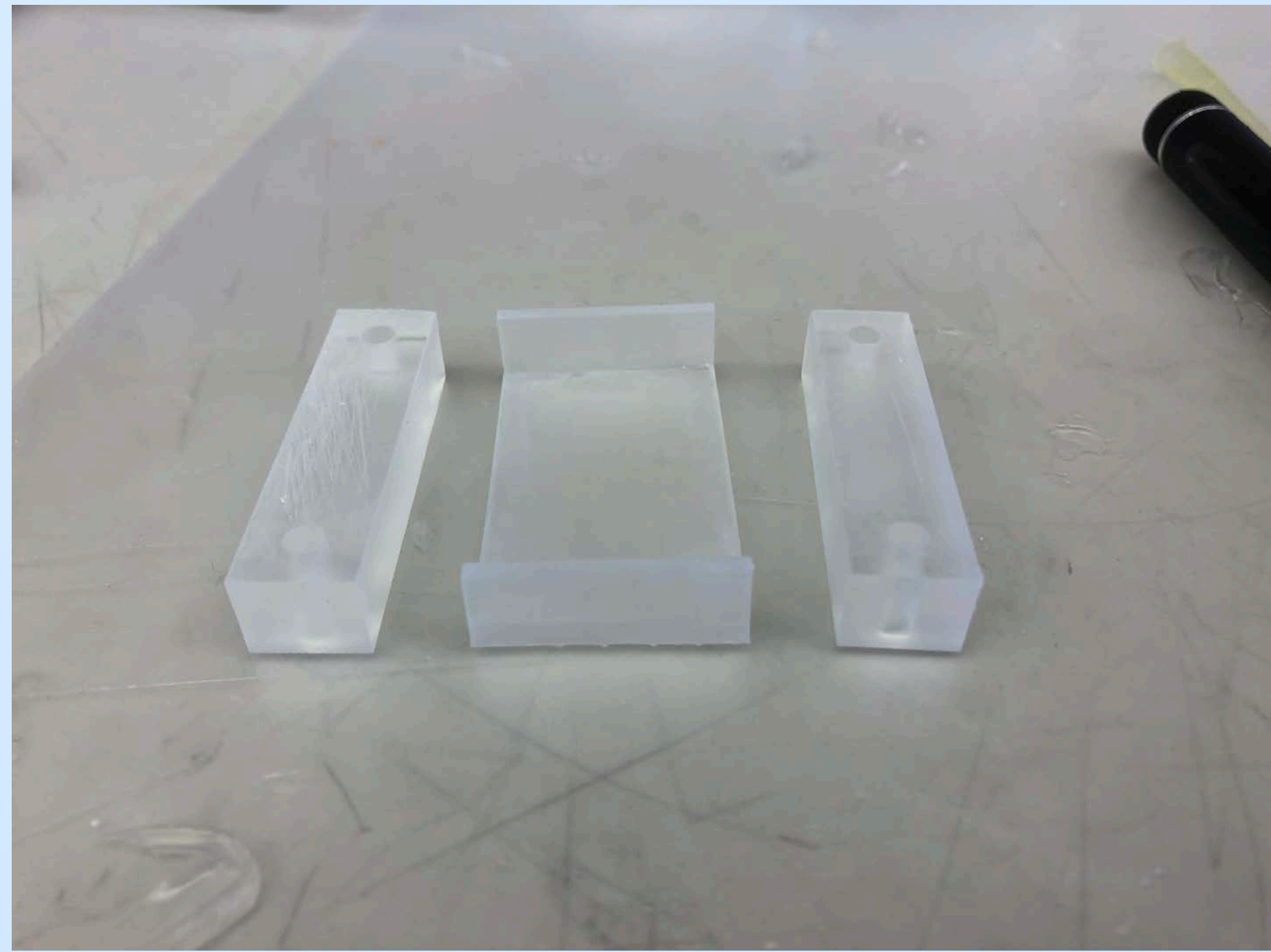
- Simmons et al. (2022) *Hydrogel Assisted Double Molding of 3D-Print Enables Prestress Regulation of Micro-Heart Muscle Physiology*. Unpublished manuscript. Preprinted on <https://doi.org/10.1101/2022.07.23.501265>
- Hirschy, A., Schatzmann, F., Ehler, E., & Perriard, J. C. (2006). Establishment of cardiac cytoarchitecture in the developing mouse heart. *Developmental biology*, 289(2), 430–441. <https://doi.org/10.1016/j.ydbio.2005.10.046>

Acknowledgements and Funding

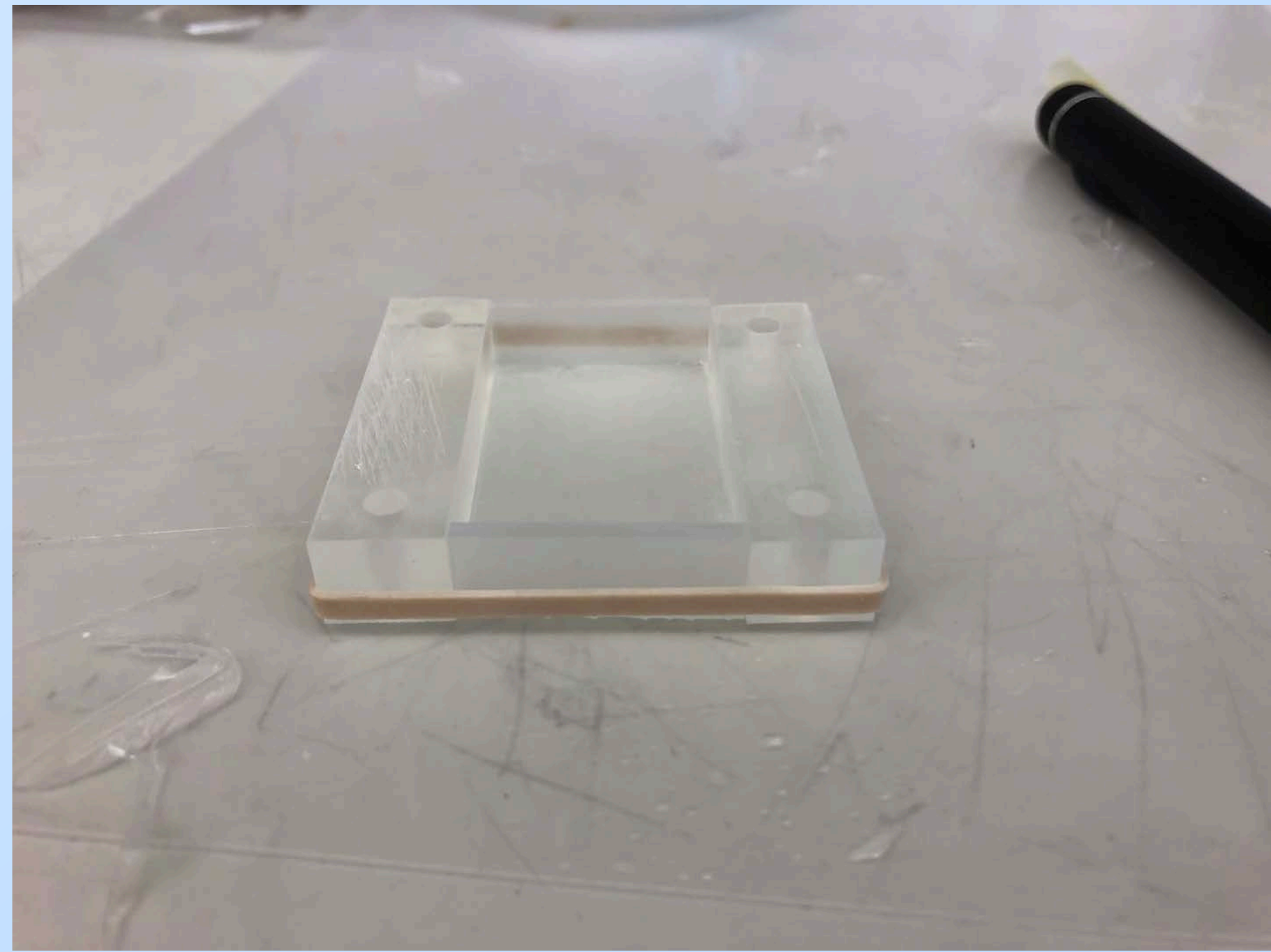
I would like to thank everyone in the Huebsch Lab, especially Lavanya Aryan and Dr. Nathaniel Huebsch. I would also like to equally thank the Center for Engineering MechanoBiology for providing me with this opportunity.

Funding Provided by CEMB and NSF





1.



2.



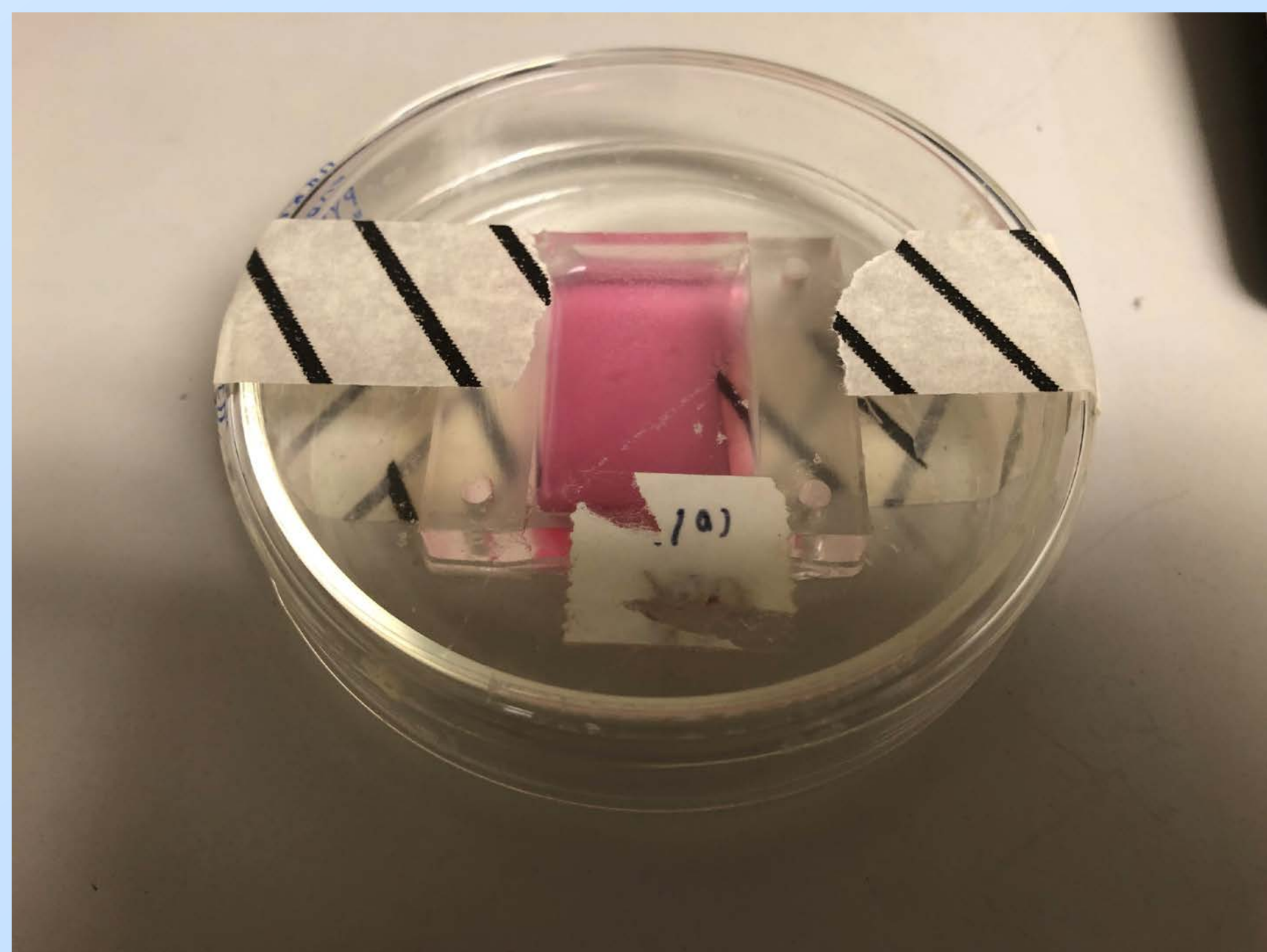
3.

48 hrs

4.



5.



6.



7.



Different Effects of Collagens I and IV on Collective Cell Migration

Kenny L. Nguyen¹, Christopher Walter², Hannah Zmuda², and Amit Pathak^{2,3}

¹Department of Biological Engineering, Louisiana State University, Baton Rouge, LA, ²Department of Biomedical Engineering, ³Department of Mechanical Engineering & Materials Science, Washington University, St. Louis, MO

Introduction: The collective migration of cells in heterogenous environments is an essential process in tissue remodeling events relating to morphogenesis, wound healing, and tumor invasion. Specifically, mammary epithelial cells (MECs) in the breast tumor microenvironment encounter heterogeneity during metastasis when invasive cells breach the basement membrane (BM), a specialized extracellular matrix (ECM) primarily composed of collagen IV meshworks, and shift to the surrounding stromal networks that are comprised of mostly collagen I fibers. The phenotypic and multicellular organization of collectively migrating MECs in response to ECM protein composition and stiffness remain inadequately investigated. In this study, we investigate how collagens I and IV at different matrix stiffnesses influence collective MEC migration.

Materials and Methods: Polyacrylamide gels of varying stiffness, 0.5 kPa (soft) and 50 kPa (stiff) were fabricated with specified ratios of acrylamide, bis-acrylamide, and ultrapure water. Each gel was coated with either rat-tail collagen I or human placenta collagen IV at concentrations of 0.05 mg/mL. Coated PA gels were incubated at 4 °C overnight (< 12 hours). Human MECs (MCF10A) with nuclear green fluorescence protein labels were seeded on collagen I or collagen IV coated PA gels (15 mm diameter) in a 12 well glass-bottom plate supplemented with cell culture medium. Collective cell migration was viewed using time-lapse microscopy, tracked using ImageJ/TrackMate, and quantified using Python.

Results and Discussion: Collective MECs migrated faster on stiff (50 kPa) substrates, regardless of the chosen ECM protein (Fig. 1A, B). In addition, MECs on stiff Collagen IV substrates had the greatest Mean Squared Displacement (MSD) while cells on soft Collagen IV substrates had the smallest MSD amongst all the ECM setups (Fig. 1C). MECs on both Collagen I- and Collagen IV-coated soft substrates show initially greater persistence, gradually decreasing to similar levels as MECs on stiff ECMs (Fig. 1D). Inversely, MECs on soft Collagen I substrates had greater persistence and directionality than on stiff Collagen I substrates (Fig. 1D, 1E). This may be due to cells quickly expanding on stiff substrates, resorting to perpendicular flow at the leading edges as they ran out of space to expand on the substrates.

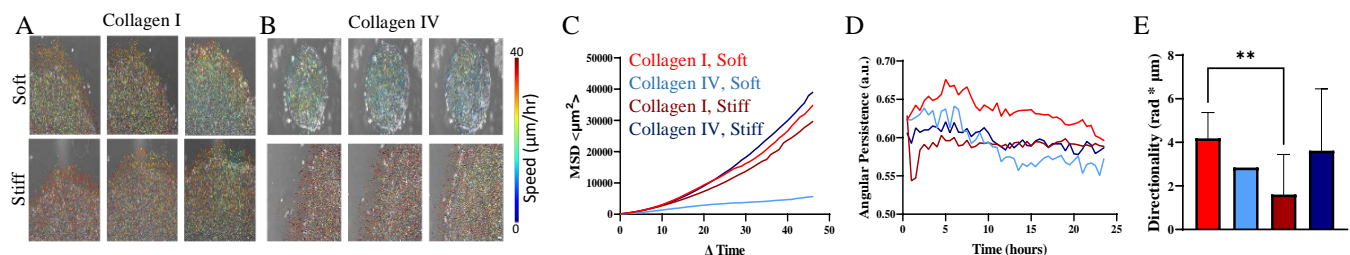


Figure 1. (A) Brightfield images of growing MEC monolayers on Collagen I and (B) Collagen IV coated matrices with quiver plot overlay showing migration speeds ($\mu\text{m}/\text{hour}$). Scale bar is $100 \mu\text{m}$. (C) MSD measures the change of a cell's position with respect to a reference position over time. (D) Angular persistence is the angle measurement of a cell's deviation from the end position. Persistence is calculated by displacement / distance. (E) Quantification of directionality through the guidance on individual cell's movement based on previous frame. Error bars represent standard deviation. $N = 1$. Statistical comparisons derived from multiple comparison one-way ANOVA. $ = P < 0.01$.**

Conclusions: In general, we found monolayer formation appeared to be more efficient on Collagen I coated substrates. However, increased substrate stiffness appears to negate these effects. MEC migration on these stiffer substrates was quicker, but much less organized and persistent. This led to tangential flow of leader cells compared to the direction of monolayer expansion as the cells ran out of space on the gel. Future directions for this work could incorporate a larger variety of ECM compositions in matrix coatings (e.g., laminin, fibronectin, Matrigel), intracellular protein analysis, and collective cell force generation via traction force microscopy.

Different Effects of Collagens I and IV on Collective Cell Migration

Kenny Nguyen¹, Christopher Walter², Hannah Zmuda², and Amit Pathak^{2,3}

¹Department of Biological and Agricultural Engineering, Louisiana State University, Baton Rouge, LA, 70803

²Department of Biomedical Engineering, Washington University, St. Louis, MO, 63130

³Department of Mechanical Engineering & Materials Science, Washington University, St. Louis, MO, 63130



Introduction

- Different phenotypes are expressed by collectively migrating cells in response to shifts in local environment from collagen IV meshworks to collagen I fibers.
- In this study, we investigate how collagens I and IV at different matrix stiffnesses influence collective mammalian epithelial cell (MEC) migration.

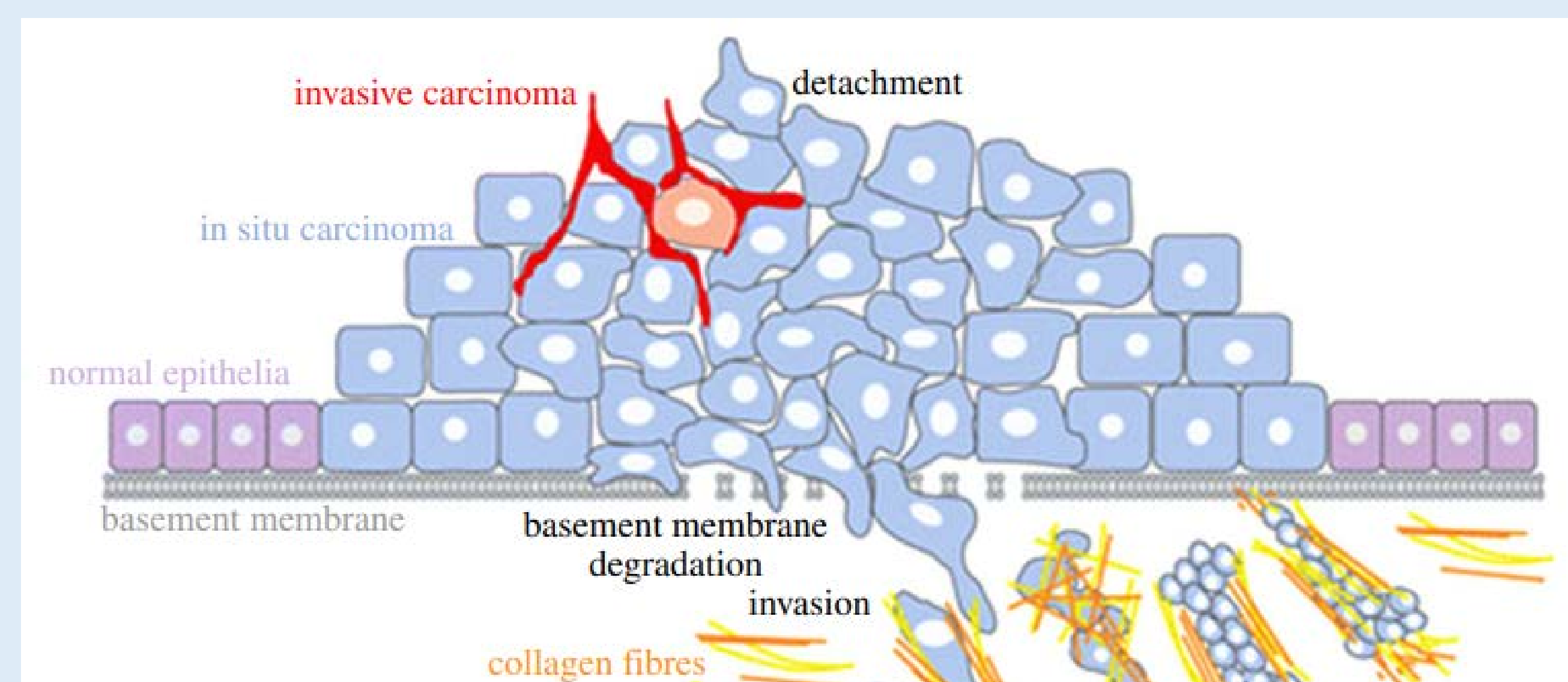


Figure 1. A schematic model of cancer leading to metastasis adapted from Djamgoz, Mustafa & Coombes, R & Schwab, Albrecht. (2014).

Methods

- Polyacrylamide gels were fabricated with specified ratios of acrylamide, bis-acrylamide, and ultrapure water for specific stiffness
 - 0.5 kPa (soft): 4% (A), 0.2% (B), 95.8% (UW)
 - 50 kPa (stiff): 10% (A), 0.15% (B), and 89.85% (UW)
- MCF-10A cells with nuclear GFP labels were seeded onto coated gels in a 12 well glass-bottom plate and allowed 24 hours to form a monolayer
- Collective cell migration is imaged using time-lapsed microscopy, tracked using ImageJ/TrackMate, and quantified using Python

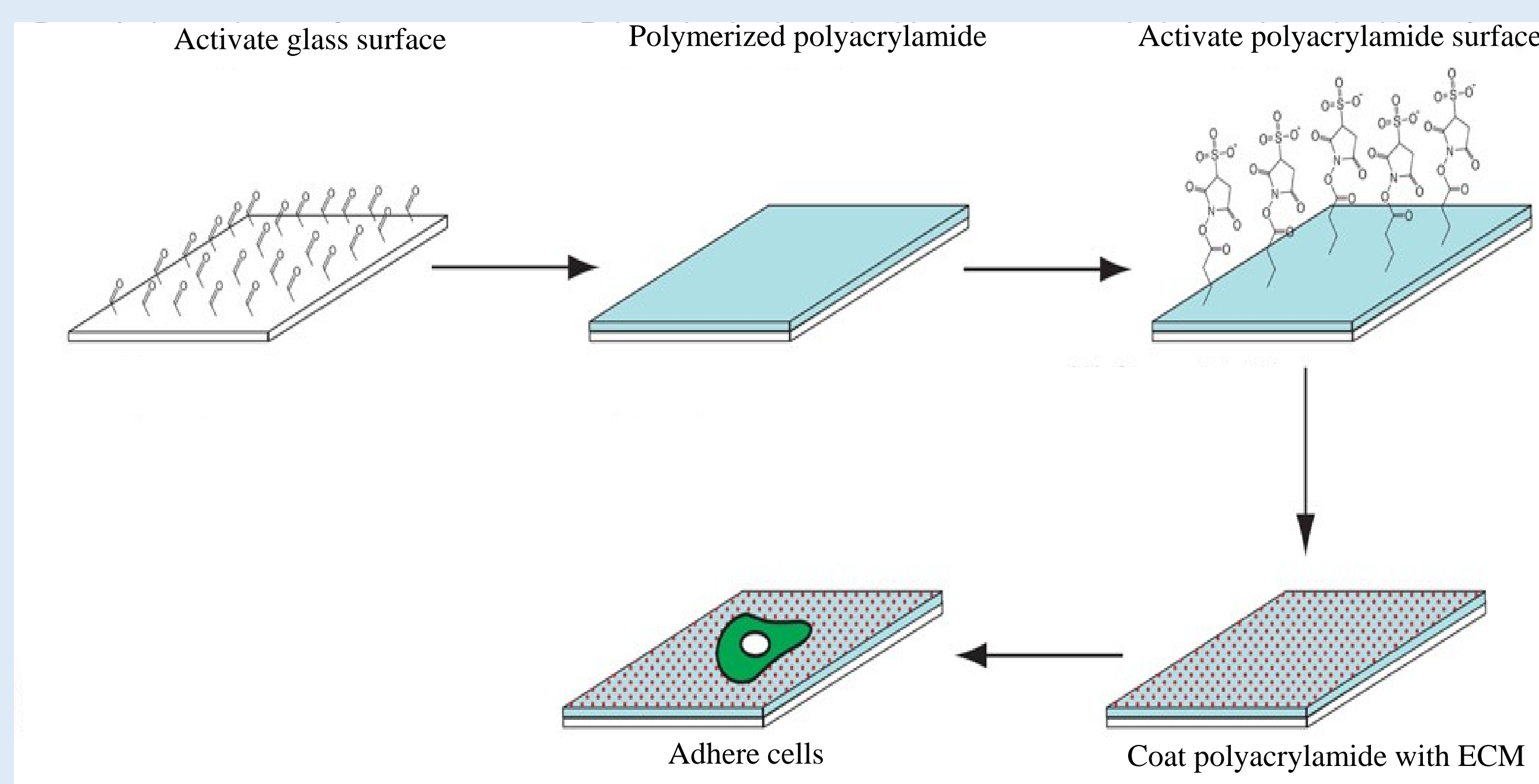


Figure 2. Schematic of gel microfabrication and cell seeding adapted from Fischer, R. S et al., (2012).

Results

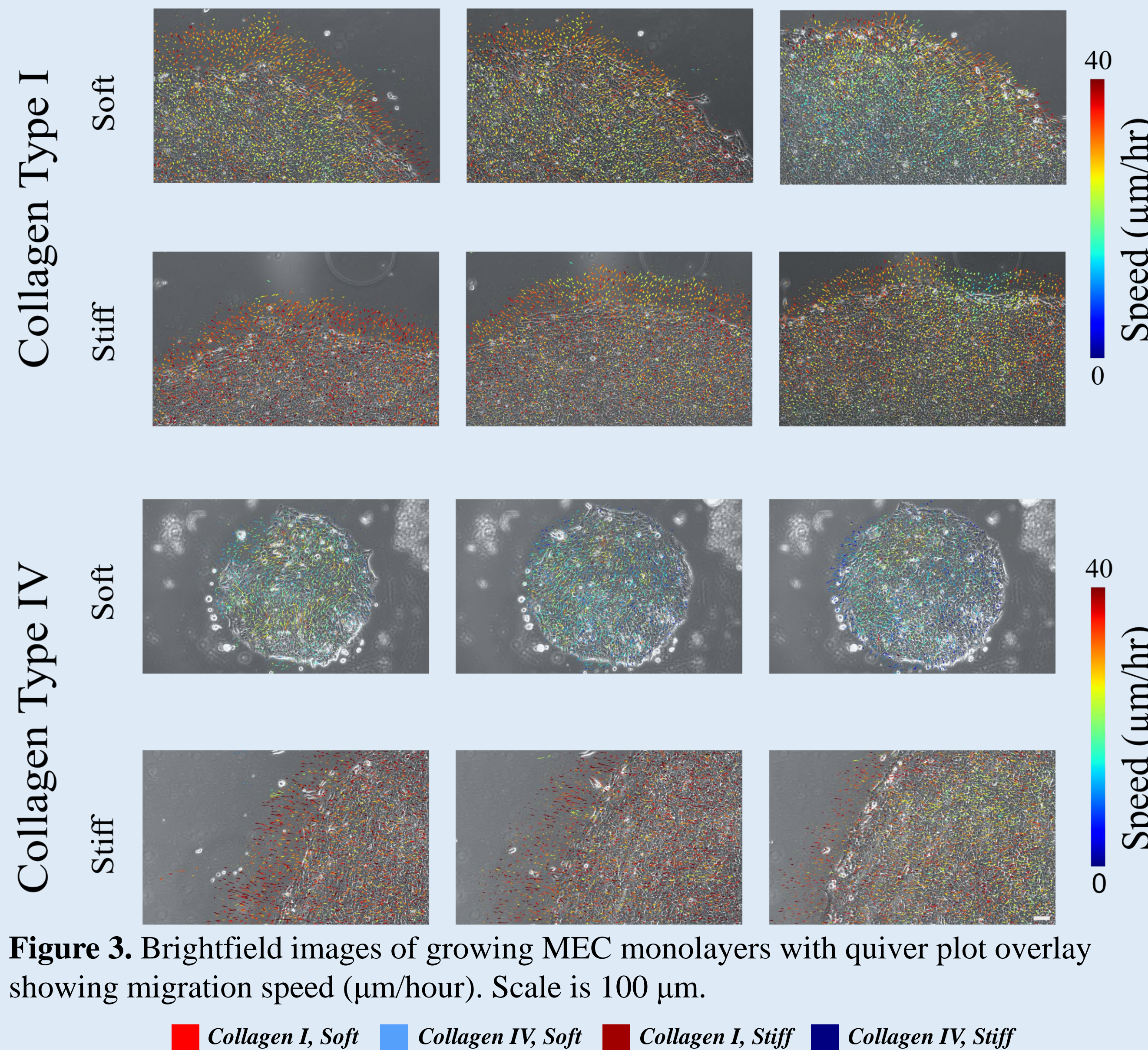


Figure 3. Brightfield images of growing MEC monolayers with quiver plot overlay showing migration speed ($\mu\text{m}/\text{hour}$). Scale is 100 μm .

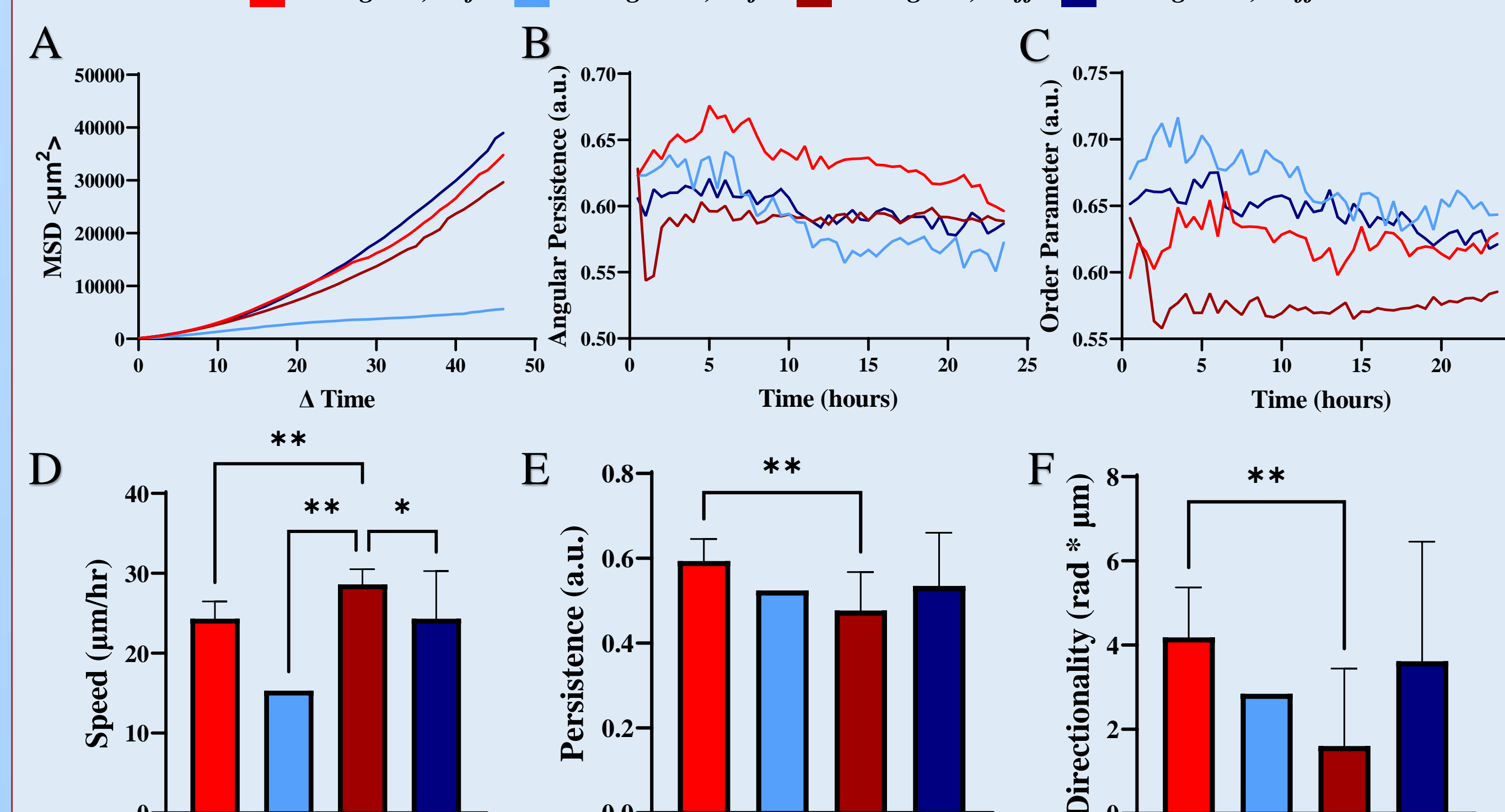
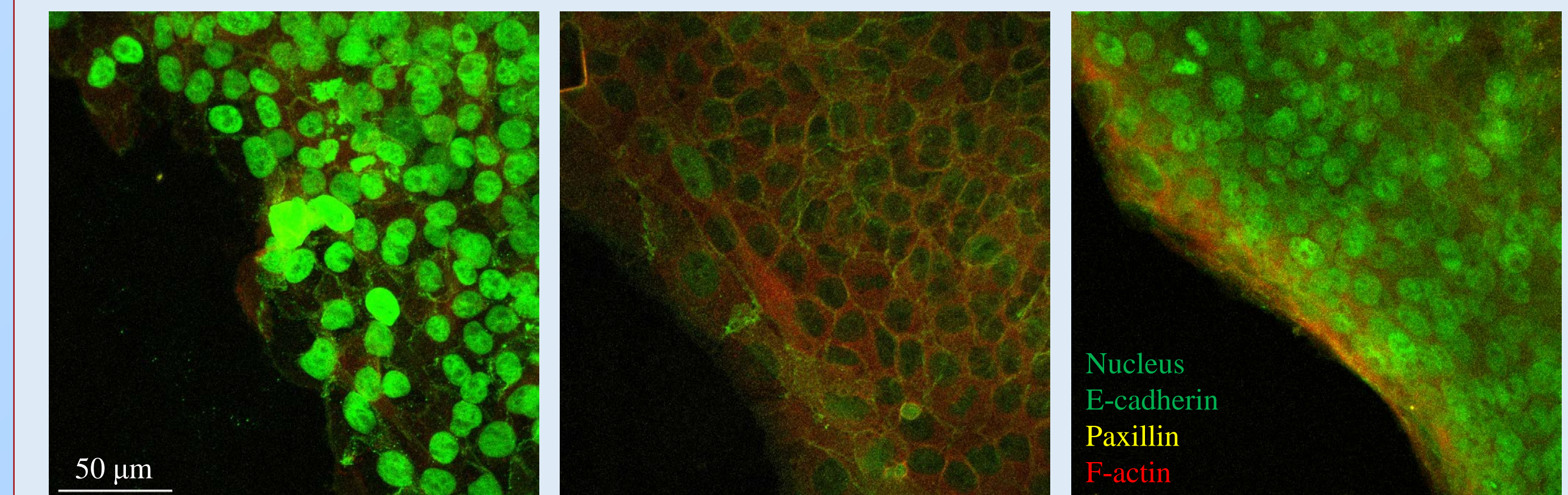


Figure 4. (A-F) Plot of (A) mean squared displacement (MSD), (B) angular persistence, (C) order parameter, (D) speed, (E) persistence, and (F) directionality. Scale Bar = SD. N=1. Statistical comparisons derived from multiple comparison one-way ANOVA. * = $p < 0.05$, ** = $p < 0.01$

- MECs show resistance to monolayer formation on **Collagen IV, soft**
- Collective MECs migrate **faster** on **stiff** (50 kPa) substrate, regardless of ECM protein
- MECs on Collagen I were **more persistent with greater directionality** on **soft** than stiff substrate
- MECs on **Collagen IV, stiff** had **greatest** Mean Squared Displacement (MSD) while **Collagen IV, soft** had the **smallest** MSD amongst all ECM setups
- MECs on both **Collagen I** and **Collagen IV, soft** show initially **greater persistence**, gradually decreasing to similar levels as MECs on **stiff** ECMs

Results (cont.)



Collagen 1, Soft

Collagen 1, Stiff

Collagen 4, Stiff

Conclusions

- Monolayer formation appears to be more efficient on Collagen I coated substrates
- Stiff ECM can minimize protein effect
- MEC migration is quicker, but less persistent and organized on stiff ECMs
- More tangential migration (perpendicular flow) at leading edge on Stiff ECMs
- Could be due to quick monolayer expansion and lack of space

Future Work

- Incorporate a larger variety of ECM protein compositions in matrix coatings (e.g., laminin, Matrigel, fibronectin)
- Immunofluorescence staining on intracellular proteins to reveal subcellular mechanisms responsible for ECM protein sensitivity during collective migration.
- Traction-force microscopy to determine effects of ECM protein on collective cell deformations and force generation

Acknowledgments

I would like to express my gratitude to the members of the Pathak lab, especially to Chris and Hannah for being great mentors and guiding me throughout the project. Also, I would like to thank Dr. Van Horn for the advice and guidance. I would like to thank P. Widder and G. Nguyen for the support.

The project is funded by the NSF Science and Technology Center for Engineering MechanoBiology (CEMB) (#1548571).

Ultraviolet Light Catalyzed Covalent Crosslinking on Benzophenone-Functionalized Cellulose Nanocrystal-Soy Protein Isolate Nanocomposites Increases Mechanical Properties and Water Resistance

Kenadie Doty^{1,2*}, Morgan Li², Jerry Wang², and Dr. Marcus Foston²
Buena Vista University¹ and Washington University in St. Louis²

Introduction: Recent interest in the production and utilization of renewable and biodegradable materials has grown in efforts to reduce industry's environmental damages. Cellulose nanocrystal (CNC) is a highly crystalline derivative of lignocellulosic and cellulosic biomasses. CNCs can be used as a reinforcement material in soy protein isolate (SPI) based nanocomposites to improve mechanical properties and water resistance. The use of benzophenone (BP) functionalized CNCs further provides promising crosslinking abilities due to its photoactivity allowing the formation of covalent crosslinking in nanocomposite materials when exposed to UV light. The goal of this study is to quantify the effects that ultraviolet (UV) activation has on BP functionalized CNC-SPI nanocomposite films through characterization of physical, structural, and mechanical properties. Understanding the effects and the interactions between the SPI matrix and CNCs is valuable for future work and potential uses of CNCs as a reinforcing material such as packaging materials, tissue engineering, and drug delivery.

Materials and Methods: CNCs were initially isolated from ground hardwood pulp through sulfuric acid hydrolysis removing amorphous regions of cellulose. After isolations, CNCs underwent TEMPO mediated oxidation to produce a surface carboxyl coating. The carboxyl-coated TEMPO-CNCs were coupled with BP to produce photoreactive BP-CNCs. Both 10% TEMPO-CNC and BP-CNC loaded SPI nanocomposite films were then produced through solvent casting and exposed to UV light to initiate cross-linking. CNCs, TEMPO-CNCs, and BP-CNCs were analyzed using Fourier transform infrared (FTIR) spectroscopy and dynamic light scattering (DLS). Carboxyl-coated and BP-functionalized CNCs underwent conductimetric titration to determine carboxyl coverage. Films underwent water absorption tests, FTIR, and mechanical testing for characterization. One-way ANOVA was employed to compare average effects among films with a 95% confidence interval for statistical significance.

Results and Discussion: Analysis of mechanical testing demonstrated a statistically significant difference between the ultimate tensile strength and Young's modulus in BP-CNC films before and after UV activation. Additionally, as seen in figure 1A, the toughness of BP-CNC films more than doubled after UV activation, having a highly significant statistical difference. The increase in mechanical properties for UV activated BP-CNC nanocomposite films suggests the presence of covalent crosslinking between the BP-CNCs and the SPI matrix. As shown in Figure 1B, water absorption testing revealed that BP-CNC films without UV activation had a weight increase of 57% while the BP-CNC films with UV activation had a weight increase of only 19.8%. This difference in water uptake is statistically significant. The decrease of water uptake in UV activated BP-CNC nanocomposite films further confirms the covalent crosslinks as these forces cause the nanocomposite to become much less permeable to water.

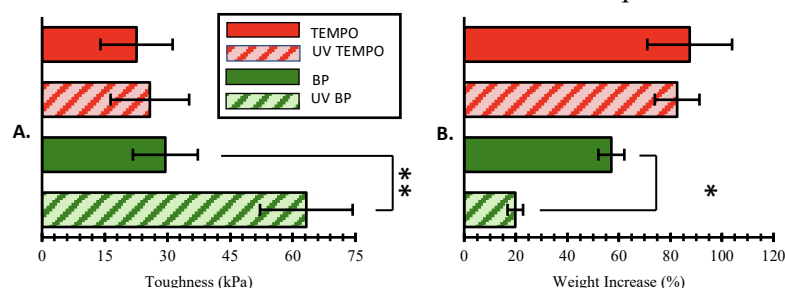


Figure 1. (A) Mechanical testing results from stress-strain curves for BP-CNC SPI and TEMPO-CNC SPI nanocomposite films. (B) Water absorption testing weight increase in BP-CNC SPI and TEMPO-CNC SPI nanocomposite films.

Conclusions: This study demonstrated that UV initiated crosslinking of BP-CNC SPI based-nanocomposite films significantly increased mechanical properties and decreased water absorption. These findings suggest that such crosslinking can improve the utility of BP-CNC nanocomposites in packaging, tissue engineering, and drug delivery applications as a renewable and biodegradable resource. Next steps in this study involves varying UV dose and the use of a photomask during UV exposure.

Acknowledgements: The Center for Engineering Mechanobiology (CEMB), Dr. Marcus Foston, Washington University in St. Louis, and the National Science Foundation (NSF).

References: Orelma, H, *et al.*, (2016). Preparation of photoreactive nanocellulosic materials via benzophenone grafting. *RSC Advances*, 6(88), 85100–85

Kenadie Doty, Morgan Li, Jerry Wang, Dr. Marcus Foston

Introduction

Recent interest in the production and utilization of renewable and biodegradable materials has grown in efforts to reduce industries environmental damages. Cellulose nanocrystal (CNC) is a highly crystalline derivative of lignocellulosic and cellulosic biomasses. This material poses extensive applications due to its availability, high surface area to volume ratio, biodegradability, and mechanical properties, including its use as a reinforcement material in soy protein isolate (SPI) based nanocomposites.

The use of benzophenone (BP) functionalized CNCs further provides promising crosslinking abilities due to its photoactivity allowing the formation of covalent crosslinking in nanocomposite materials when exposed to UV light. The goal of this study is to **evaluate the affects that ultraviolet (UV) activation has on BP functionalized CNC-SPI nanocomposite films** through characterization of physical, structural, and mechanical properties.

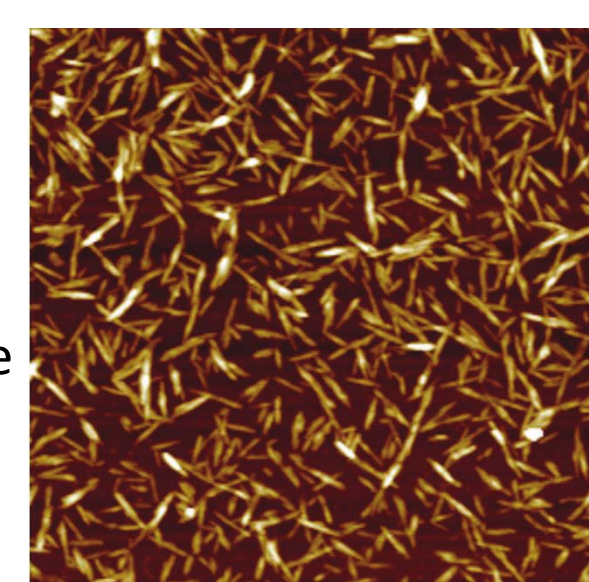


Figure 1: Atomic-force microscopy (AFM) image of CNCs.

Results (Characterization of CNCs)

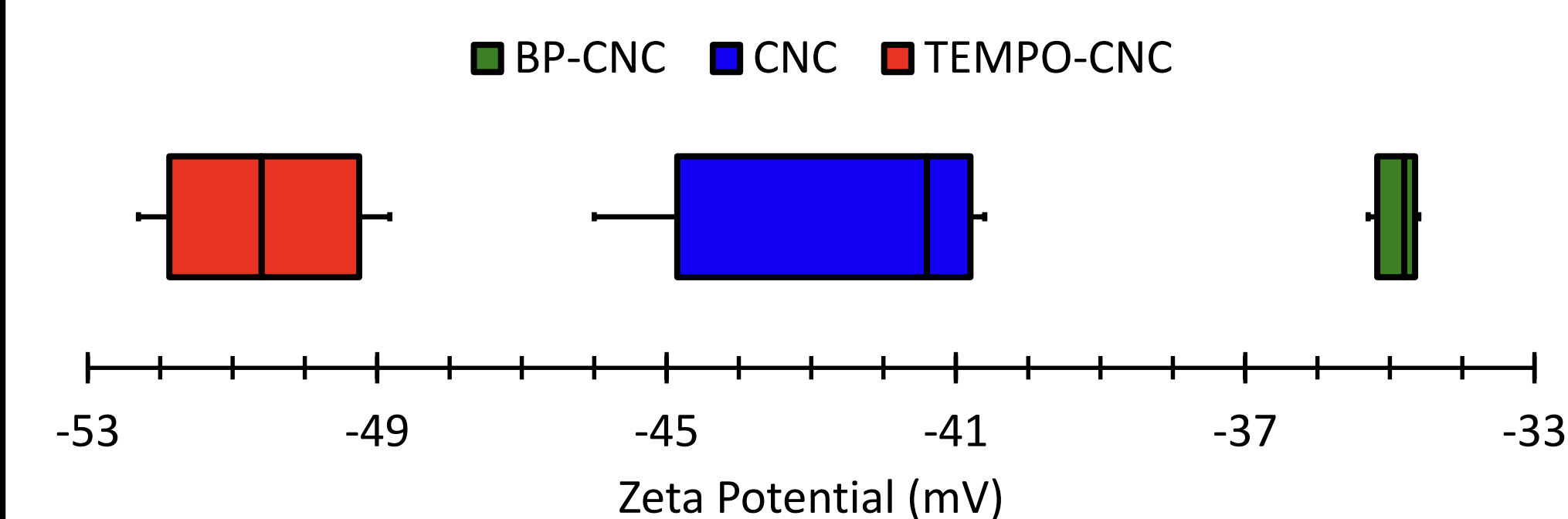


Figure 2: Zeta Potential Values measured by DLS for CNCs (-42.7 mV), TEMPO-CNCs (-50.6 mV), and BP-CNCs (-34.9 mV).

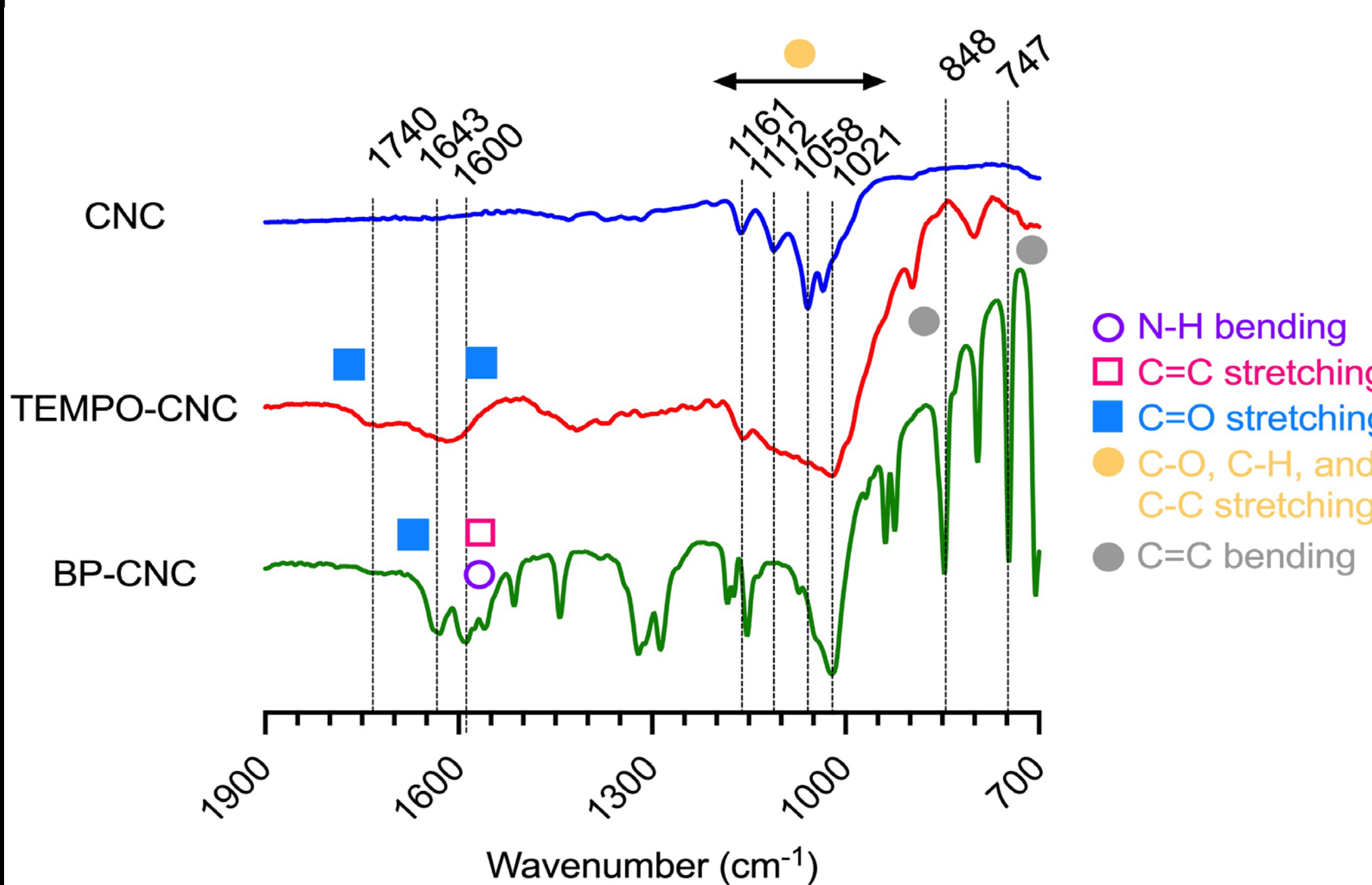


Figure 3: FTIR spectra comparing CNCs, TEMPO-CNCs, and BP-CNCs. Peaks not present in CNCs at 1600 cm⁻¹ and 1740 cm⁻¹ appear in TEMPO-CNCs and BP-CNCs. Comparing TEMPO-CNCs to BP-CNCs, new peaks appear for BP-CNCs at 1643 cm⁻¹, 848 cm⁻¹ and 747 cm⁻¹.

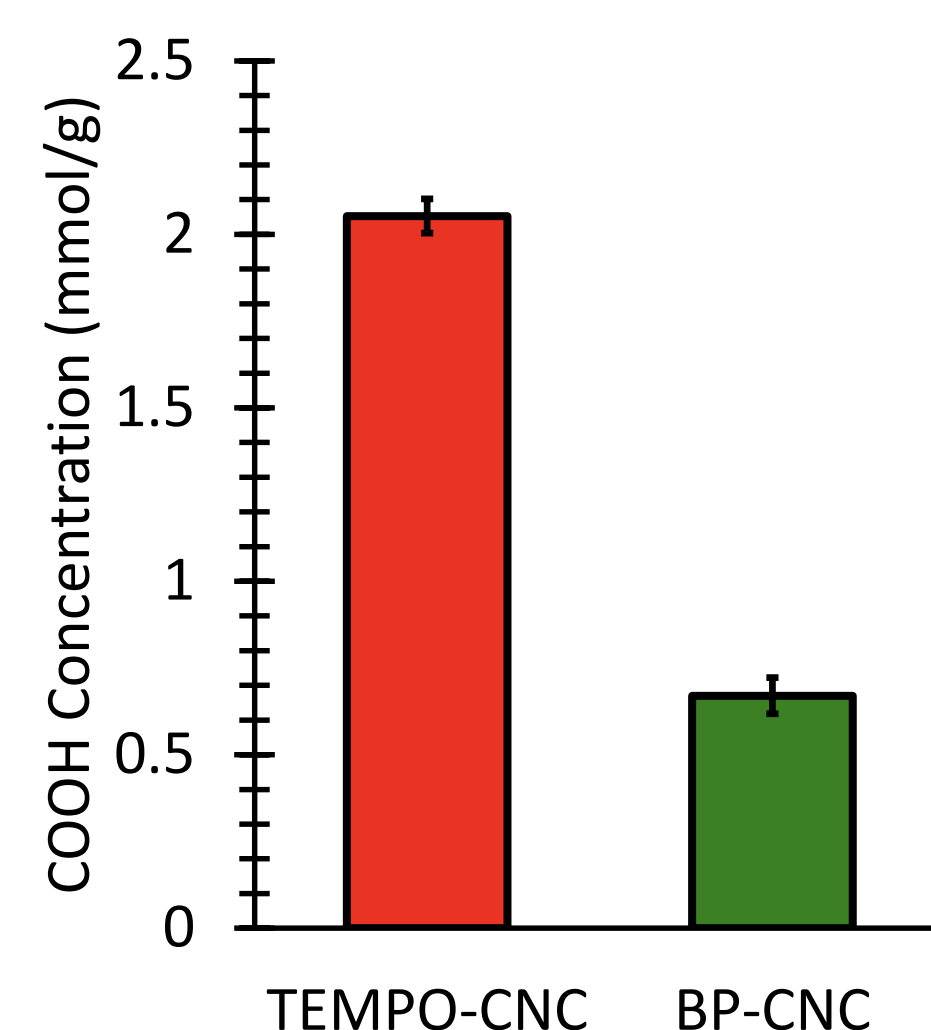
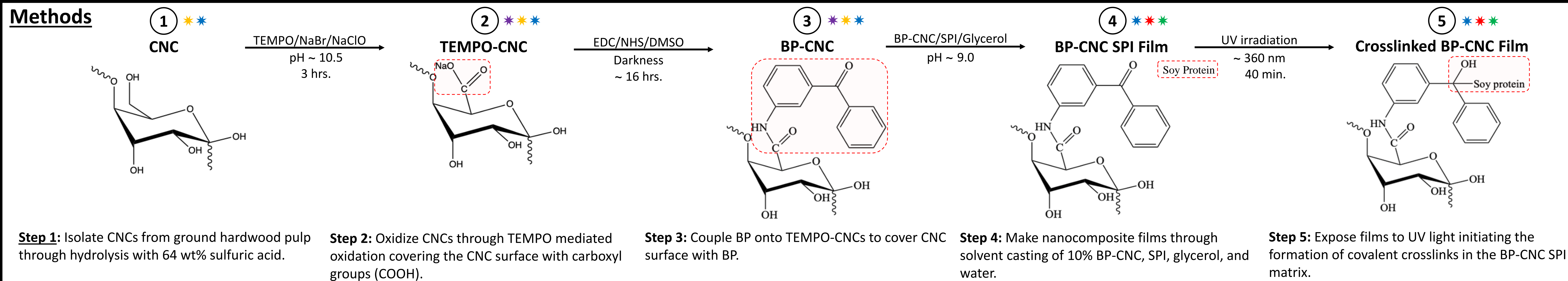


Figure 4: Carboxylic acid group contents in TEMPO-CNCs (2.05 mmol/g) and BP-CNCs (0.67 mmol/g).

Methods



Characterization Methods

- Conductometric Titration:** Quantifies Carboxyl content of CNCs.
- Dynamic Light Scattering (DLS):** Quantifies zeta potential and estimated size of CNCs.
- Fourier Transform Infrared Spectroscopy (FTIR):** Identifies chemical composition of sample.
- Mechanical Testing:** Quantifies ultimate tensile strength, toughness, and Young's modulus of material.
- Water Absorption Testing:** Quantifies water uptake of films.

Results (Characterization of CNC Films)

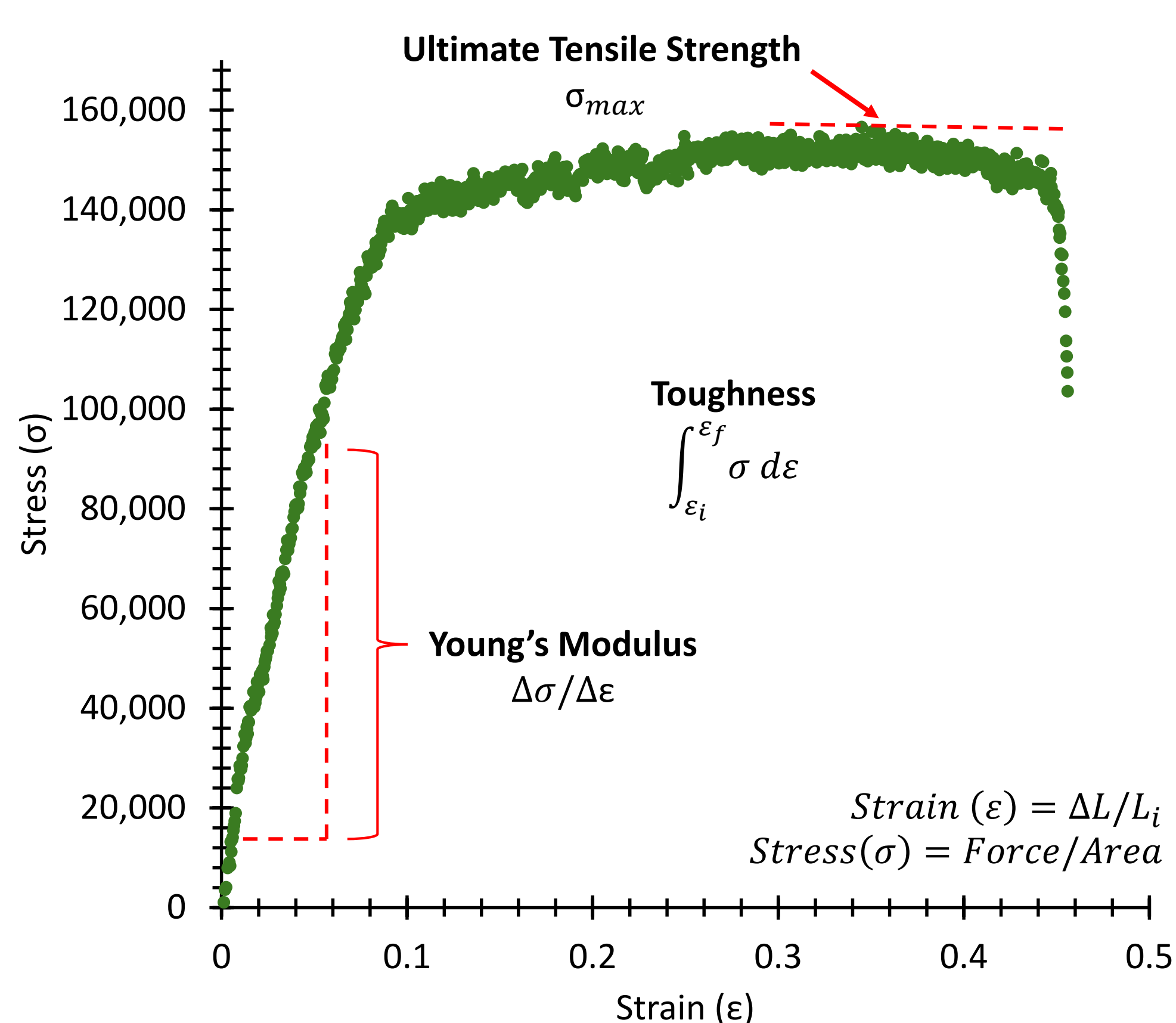


Figure 5: Mechanical testing stress-strain curve from BP-CNC SPI film with ultimate tensile strength, toughness, and Young's modulus labels and derivations.

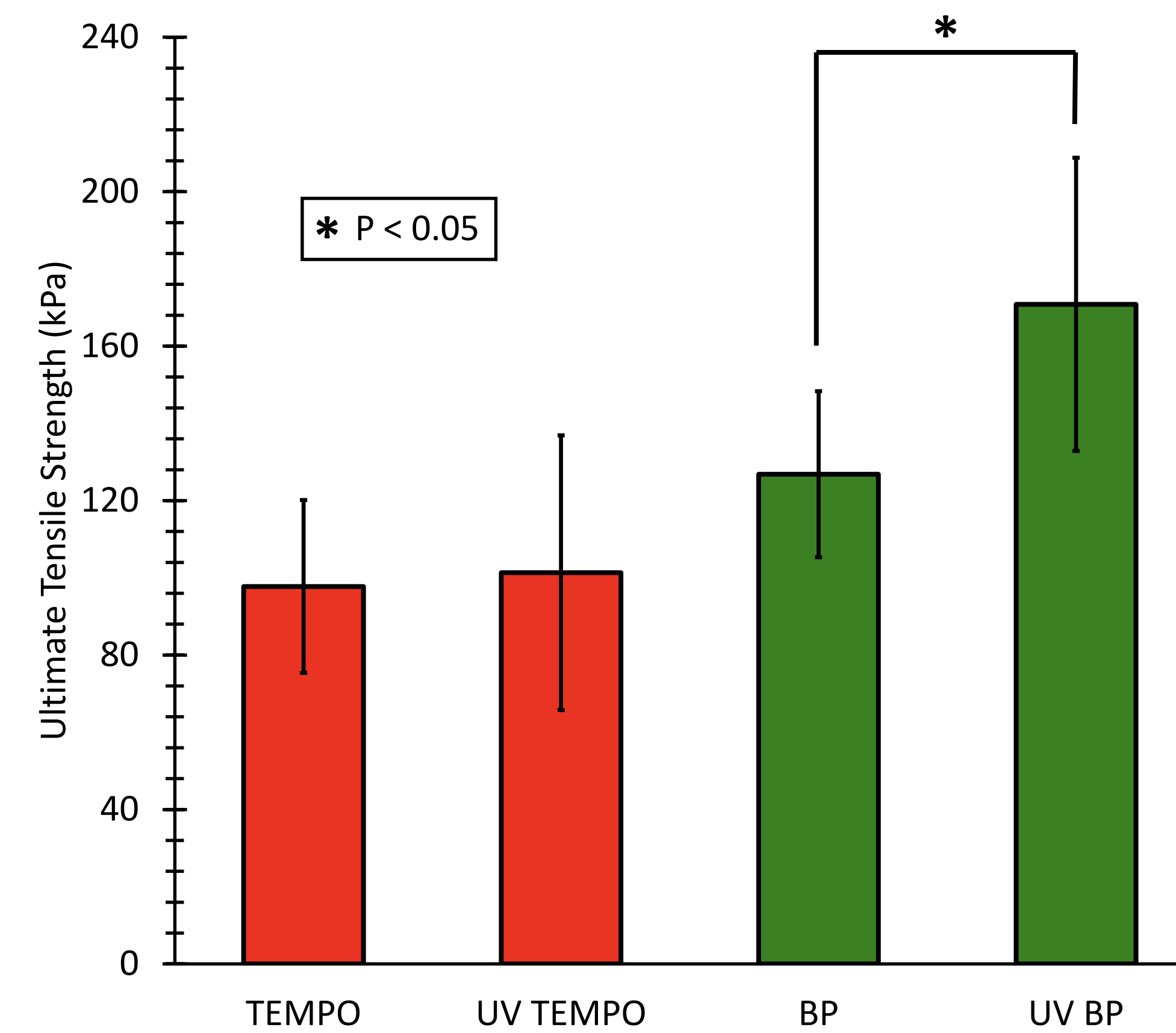


Figure 6: Ultimate tensile strength of TEMPO-CNC films (97.8 kPa without UV, and 101.4 kPa with UV) and BP-CNC films (126.8 kPa without UV, and 170.8 kPa with UV).

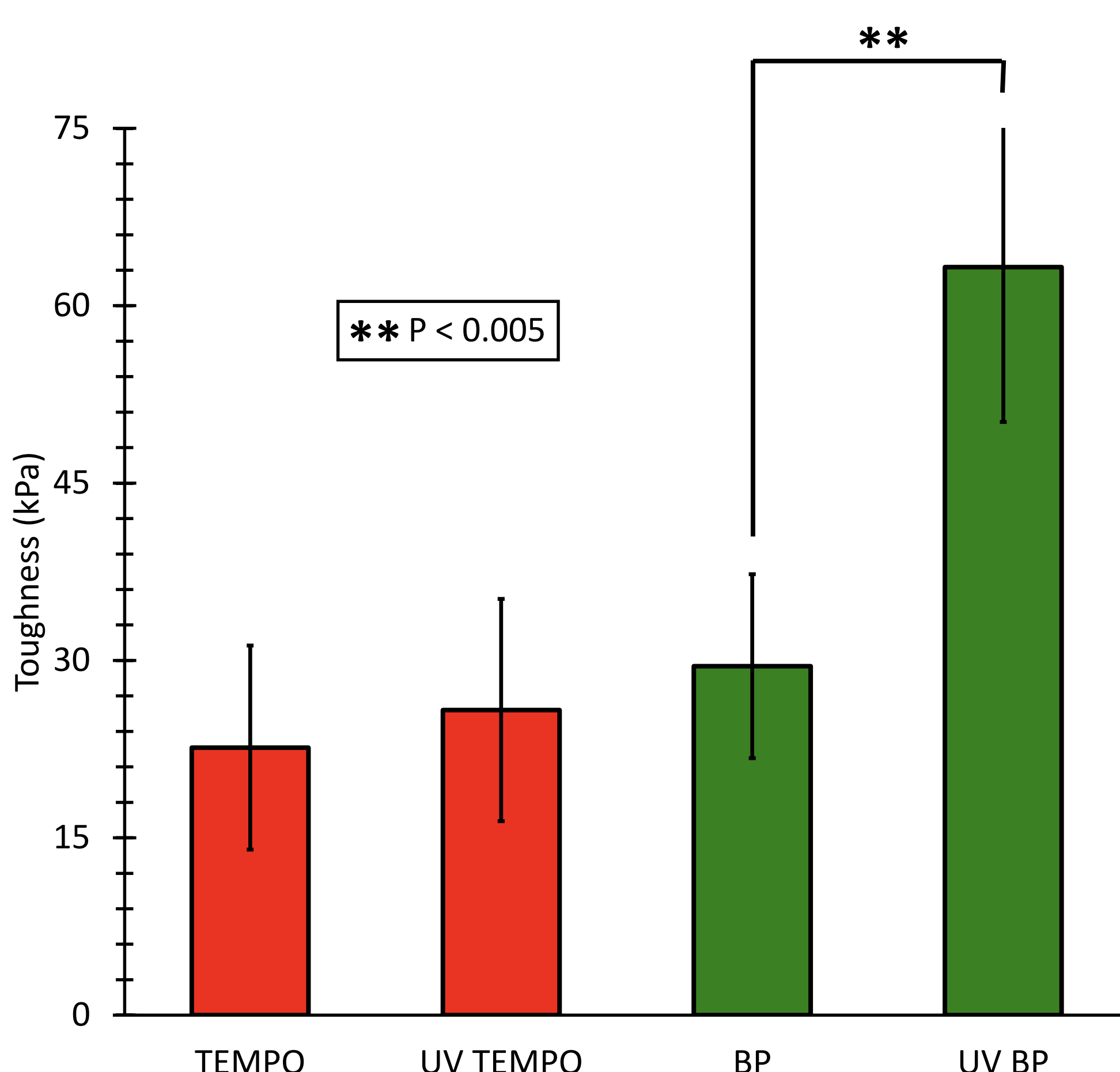


Figure 7: Toughness of TEMPO-CNC films (22.7 kPa without UV, and 25.81 kPa with UV) and BP-CNC films (29.5 kPa without UV, and 63.3 kPa with UV).

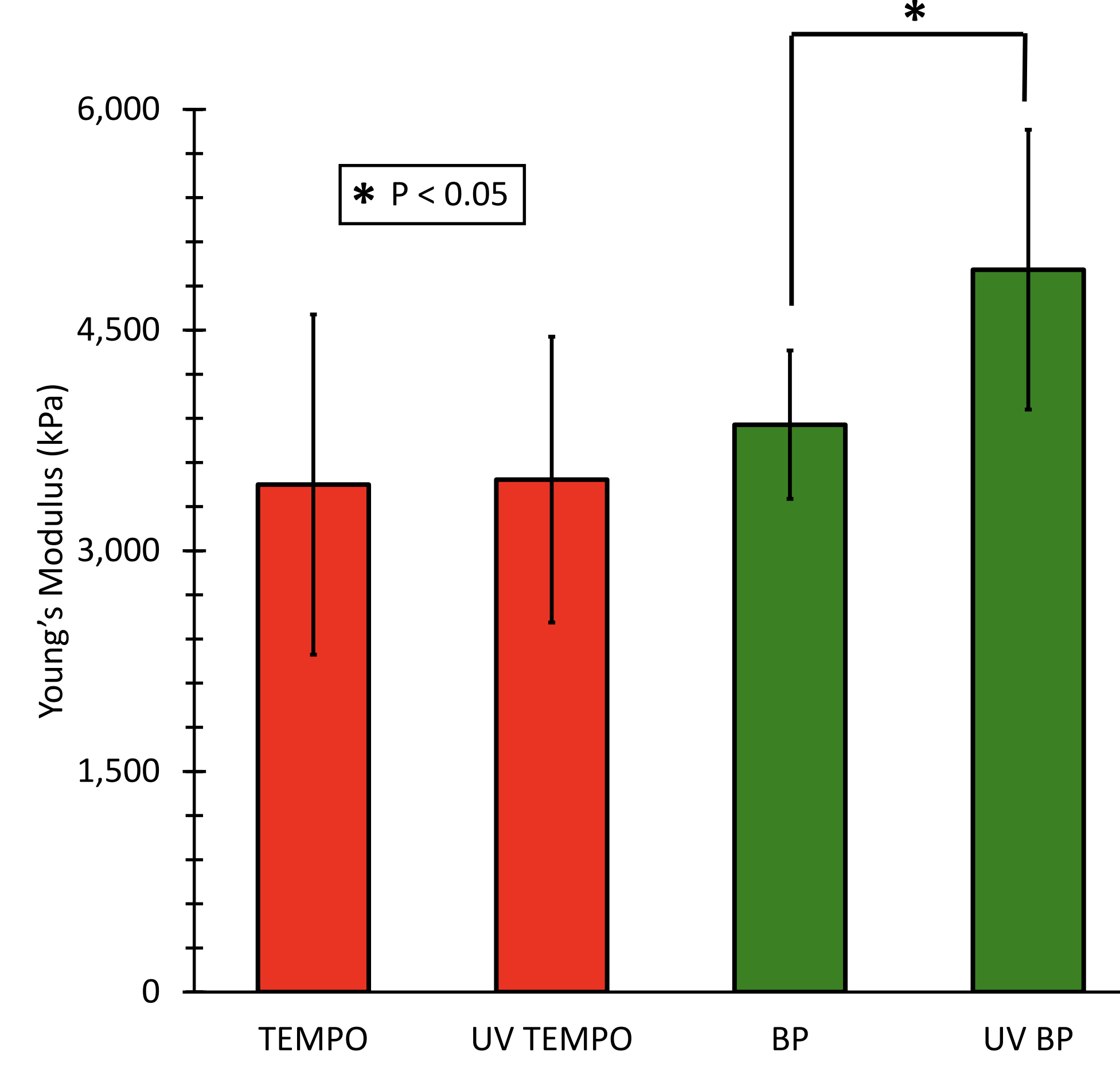


Figure 8: Young's Modulus of TEMPO-CNC films (3,450 kPa without UV, and 3,484 kPa with UV) and BP-CNC films (3,857 kPa without UV, and 4,911 kPa with UV).

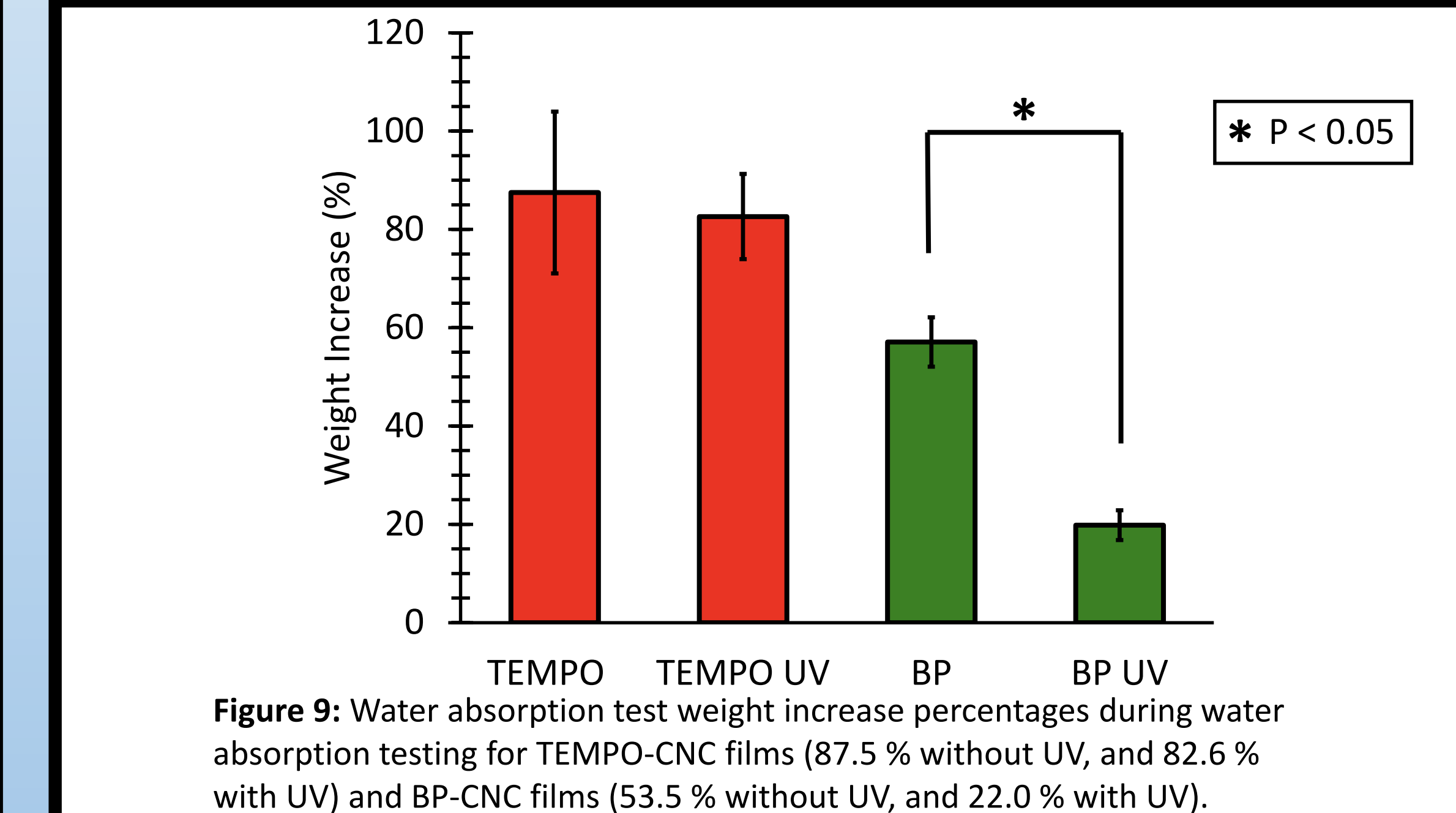


Figure 9: Water absorption test weight increase percentages during water absorption testing for TEMPO-CNC films (87.5% without UV, and 82.6% with UV) and BP-CNC films (53.5% without UV, and 22.0% with UV).

Discussion

Mechanical Testing:

- Significant increase of both ultimate tensile strength and Young's modulus in BP-CNC films after UV activation and a highly significant increase of toughness in BP-CNC films after UV activation.
- The increase in mechanical properties for UV activated BP-CNC nanocomposite films suggests the presence of covalent crosslinking between the BP-CNCs and the SPI matrix.

Water Absorption Testing:

- Significant decrease in water uptake of BP-CNC films after UV activation.
- The decrease of water uptake in UV activated BP-CNC nanocomposite films further confirms the covalent crosslinks as these forces cause the nanocomposite to become much less permeable to water.

Understanding the effects and the interactions between the SPI matrix and CNCs is valuable for future work and potential uses of CNCs as a reinforcing material.

Acknowledgements

I would like to thank The Center for Engineering MechanoBiology (CEMB), Dr. Marcus Foston, Washington University in St. Louis, and the National Science Foundation (NSF).

References

- Orelma, H., Vuoriluoto, M., Johansson, L. S., Campbell, J. M., Filpponen, I., Biesalski, M., & Rojas, O. J. (2016). Preparation of photoreactive nanocellulosic materials via benzophenone grafting. *RSC Advances*, 6(88), 85100–85106. <https://doi.org/10.1039/c6ra15015b>
- Tanpichai, S., & Oksman, K. (2018). Aligned porous-structured poly(vinyl alcohol) foams with cellulose nanocrystals. *AIP Conference Proceedings*. <https://doi.org/10.1063/1.5053183>
- Zhang, S., Xia, C., Dong, Y., Yan, Y., Li, J., Shi, Q., & Cai, L. (2016). Soy protein isolate-based films reinforced by surface modified cellulose nanocrystal. *Industrial Crops and Products*, 80, 207-213. <https://doi.org/10.1016/j.indcrop.2015.11.070>
- Full list of references available upon request.

Follistatin is Required for Mass Maintenance but Not Partial Force Recovery Following Muscle Injury

Siena J. Smith^{1,2*}, Jacob C. Parson², Gretchen A. Meyer²

¹University of Michigan-Dearborn, Dearborn, MI ²Washington University in St. Louis, St. Louis, MO

Introduction: Follistatin (Fst) is an activin-binding protein that blocks myostatin, a muscle growth inhibitor. Follistatin overexpression results in increased muscle mass and torque production and improves muscle healing after injury. However, follistatin deletion is neonatal lethal so little is known about its requirement for adult muscle homeostasis. Thus, its importance for myogenesis is clear but its role in muscle regeneration and injury response is unknown. The goal of this study was to assess recovery and early hypertrophic signaling in the tibialis anterior muscle (TA) of inducible follistatin-knockout mice at the tissue and single cell levels and evaluate whether follistatin plays a role in the early phase injury response of adult muscle.

Materials and Methods: Tamoxifen induced follistatin knockout mice (FstKO) were generated by crossing *Esr1-Cre* mice with *Fst* floxed mice and compared to littermate controls (WT). Tamoxifen was administered via intraperitoneal injection for 5 days followed by a 2-week washout. After treatment, all mice were subjected to a 2-day TA contraction protocol with a day of rest in between. During the protocol, the knee of an anesthetized mouse was clamped with the ankle secured to a rotating footplate of a force transducer measuring dorsiflexion torque. Needle electrodes were precisely placed to stimulate the peroneal nerve. Electrical impulses were administered every 300 ms at 300 Hz to stimulate eccentric (ECC) contractions (20° of dorsiflexion) to induce overload injury on one leg and isometric (ISO) contractions as a non-injurious control on the other. This was done in 10 sets of 6 contractions with 50 seconds of rest between sets for each leg. Following the last contraction bout, puromycin was injected intraperitoneally. Muscle harvest of the control supraspinatus and both TAs occurred exactly one hour later. Harvested muscles were flash frozen for cryosectioning, H&E staining, and western blotting.

Results and Discussion: Pre-test torques were not different between FstKO and WT mice. Torque dropped 60-70% post contraction bout and recovered to ~50% after one day of rest for both ECC and ISO (Fig. 1a/b). There was no significant genotype/time interaction, indicating that Fst deletion did not impact injury response. The TA masses after both contraction types were ~15% lower in FstKO mice than WT (Fig. 1c). This deficit was consistent in the masses of unexercised FstKO and WT mice as well. Western blotting results trended towards increased puromycin incorporation in exercised TAs vs. supraspinatus muscles without a significant difference between genotypes (Fig. 1d). ~20% more necrosis occurred in eccentrically contracted than isometrically contracted muscle with more degeneration occurring in FstKO muscle than WT (Fig. 1e).

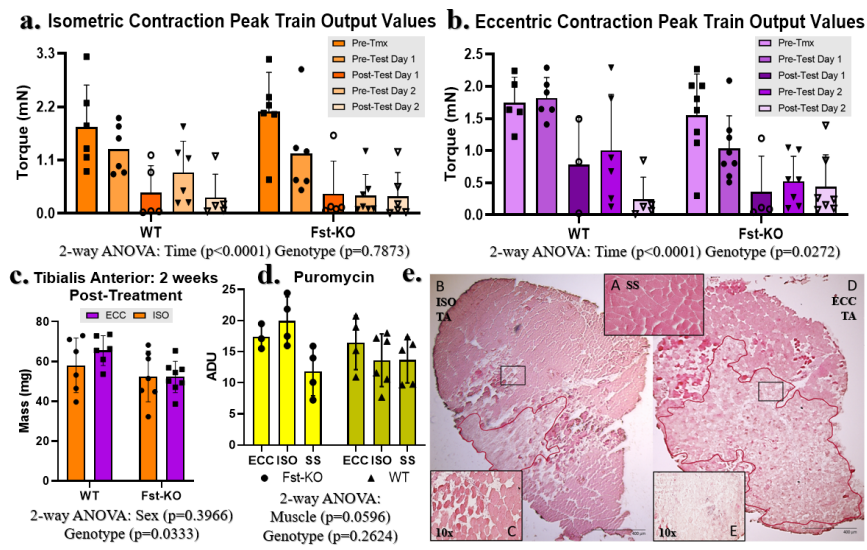


Figure 1. (a/b) Average force of tetanic contractions throughout protocol. (c) Exercised TA masses post treatment/pre-testing. (d) Puromycin western blot quantification. (e) H&E staining with red outlined necrosis and magnified regions.

Conclusions: Based on these findings, follistatin is required for mass maintenance but not force production in the early injury response of adult muscle. Since partial force recovery occurred, some muscle recovery was possible even without the protein. Clinically, speculation exists that sarcopenia, the muscle loss and weakness in humans that comes with age, could be partially attributed to a reduction in follistatin which circulates less with age. However, due to experimental variability, this study was underpowered to detect small differences between the follistatin-knockout and wild type genotypes. Future work would include reducing the damage done by the needle electrodes, considering a different injury model, and increasing numbers per group to increase statistical power.

Follistatin is Required for Mass Maintenance but Not Partial Force Recovery Following Muscle Injury

Siena J. Smith^{1,2}, Jacob C. Parson², Gretchen A. Meyer²

¹University of Michigan-Dearborn, Dearborn, MI
²Washington University in St. Louis, St. Louis, MO



INTRODUCTION

Follistatin (Fst) is an activin-binding protein that blocks myostatin, a muscle growth inhibitor. Overexpression of follistatin results in increased muscle mass and torque production and improves muscle healing after injury. However, follistatin is neonatal lethal so almost no work has been done with follistatin deficient mice. Therefore, the importance in myogenesis is clear but it's role in muscle regeneration and injury response is unknown. The goal of this experiment was to assess the hypertrophic response of the tibialis anterior (TA) muscle in the absence of follistatin at the tissue and single cell levels and evaluate whether follistatin is required for muscle homeostasis.

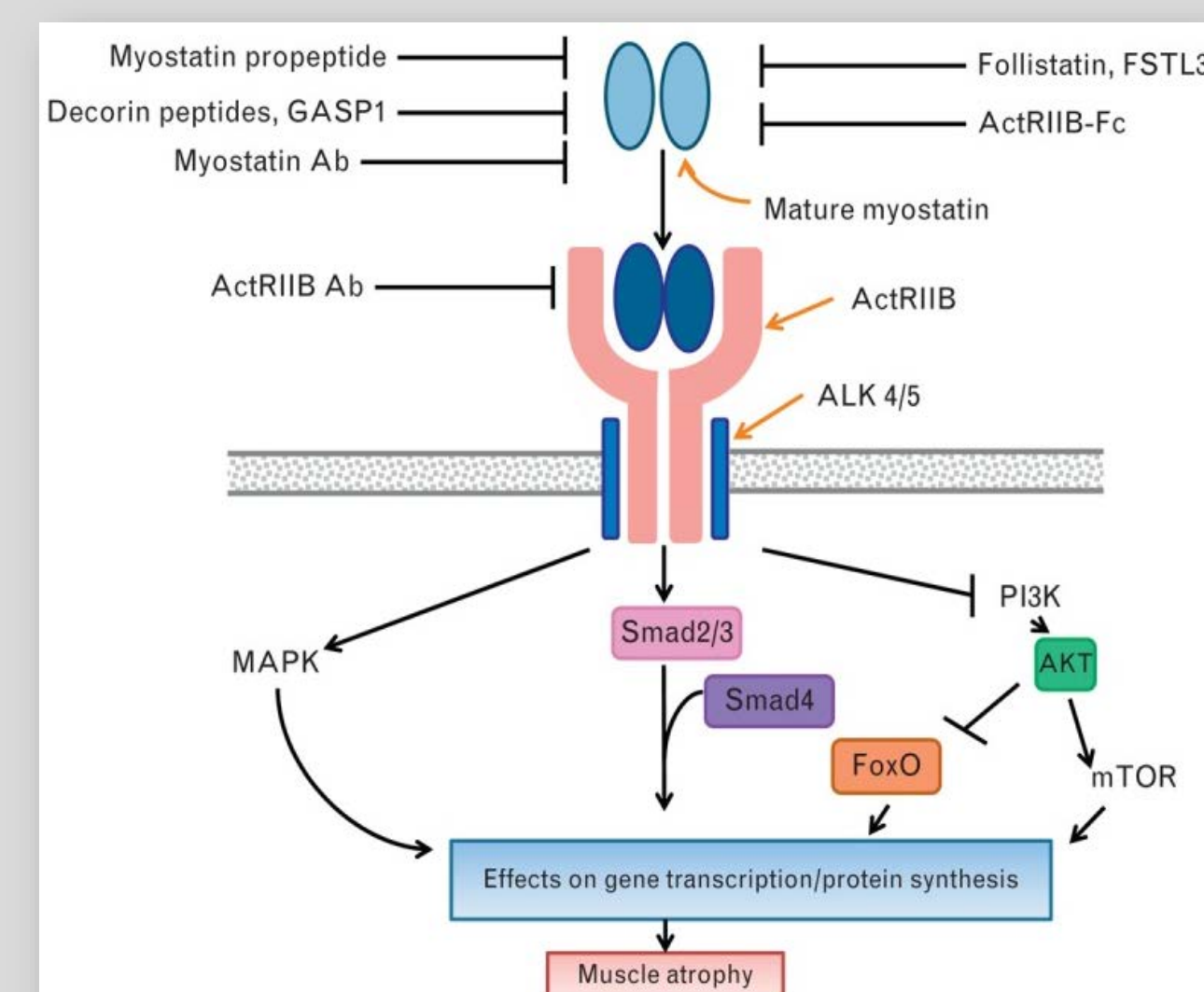


Figure 1. Myostatin Signaling Pathway
Smith et al. Curr Opin Support Palliat Care. 2013 Dec;7(4):352-60

METHODS

Animal Model: B6N.129S6-Esr1^{tm1.1(cre)And/J+/-x Fst^{fl/fl}}

8 Fst-KOs
6 littermate controls (WT)

This experiment was based on several existing procedures. The treatment timeline applies to each mouse. The relevant harvested tissues were the supraspinatus (SS/control) and both TAs.

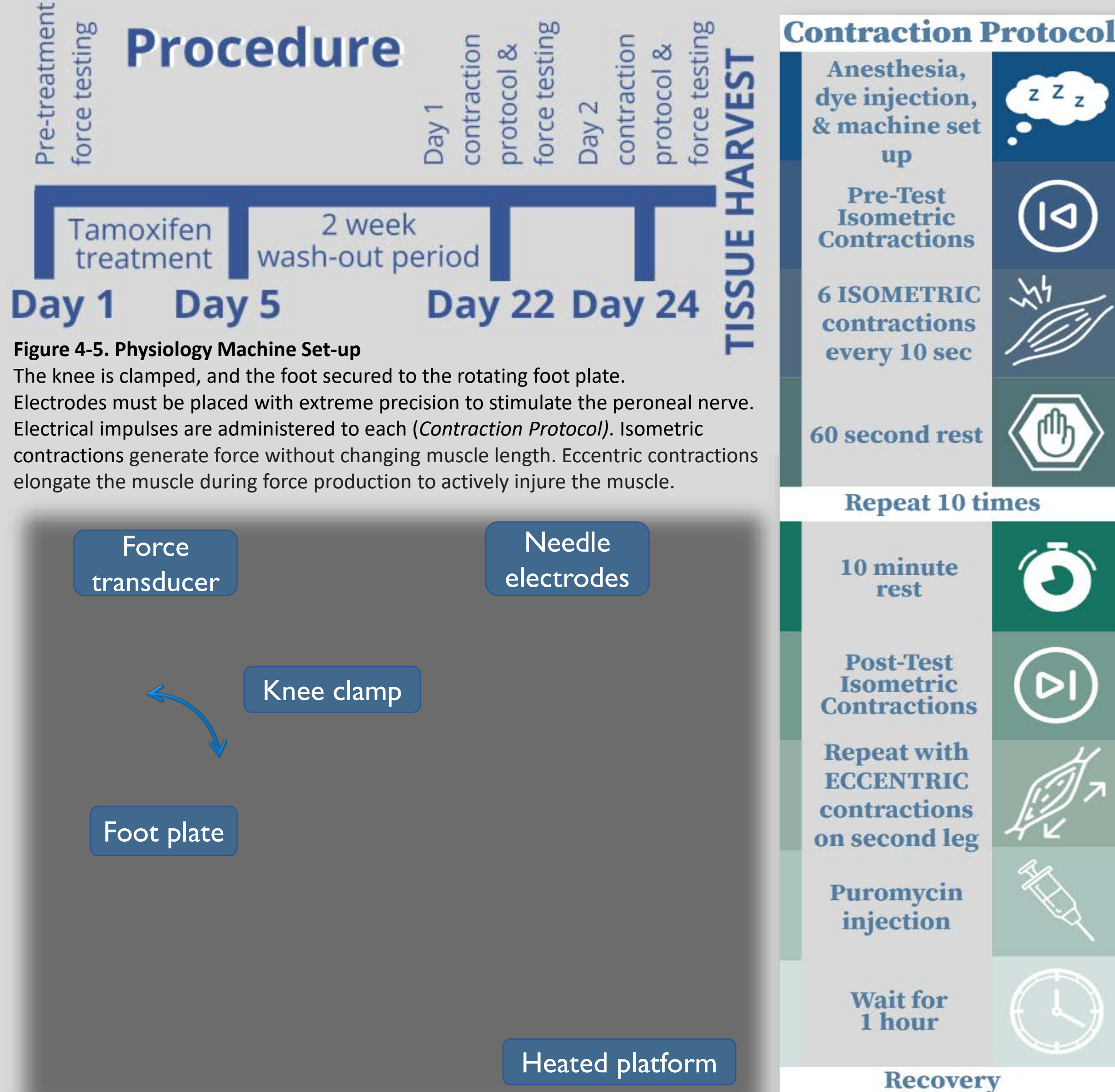
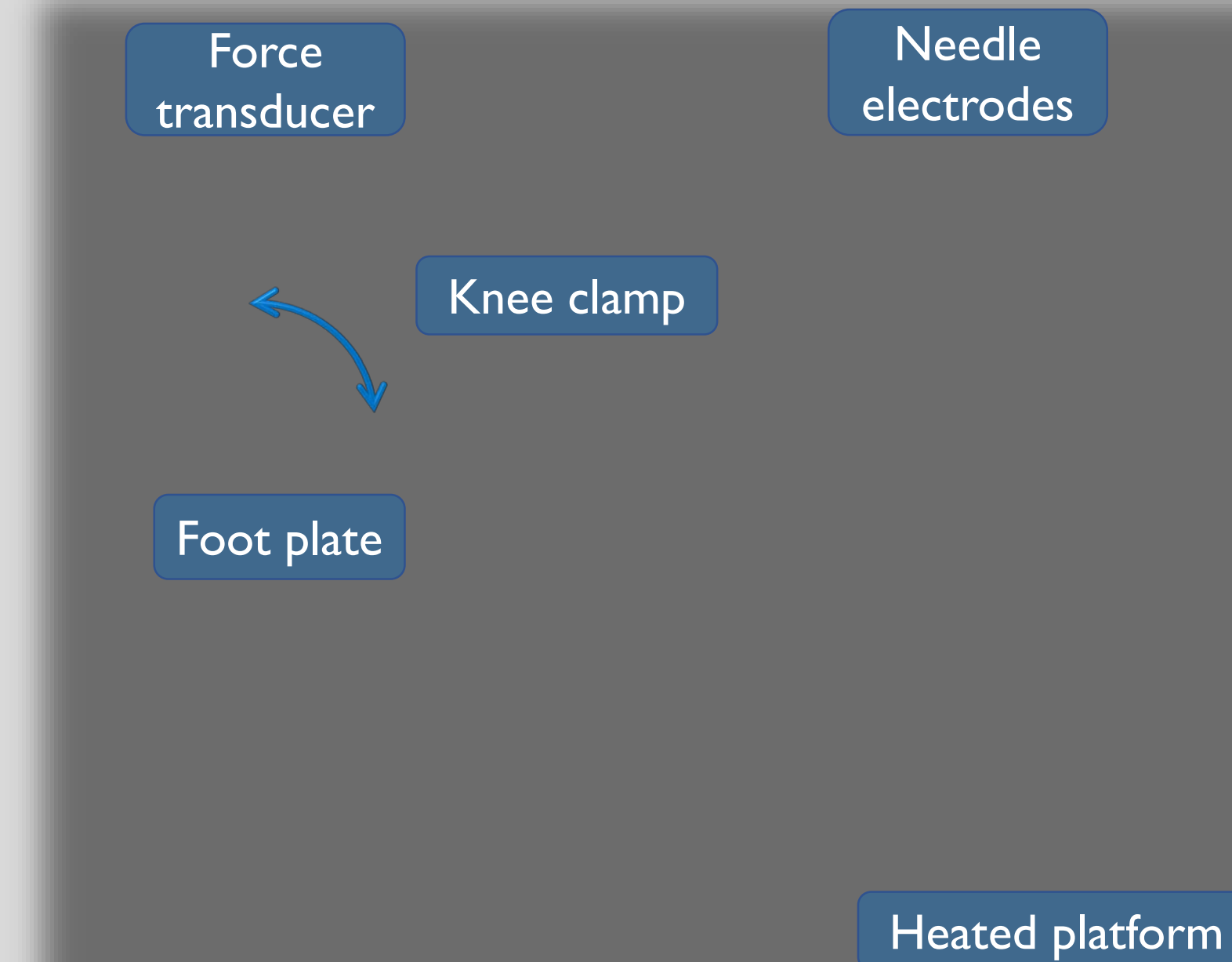


Figure 4-5. Physiology Machine Set-up
The knee is clamped, and the foot secured to the rotating foot plate. Electrodes must be placed with extreme precision to stimulate the peroneal nerve. Electrical impulses are administered to each (Contraction Protocol). Isometric contractions generate force without changing muscle length. Eccentric contractions elongate the muscle during force production to actively injure the muscle.

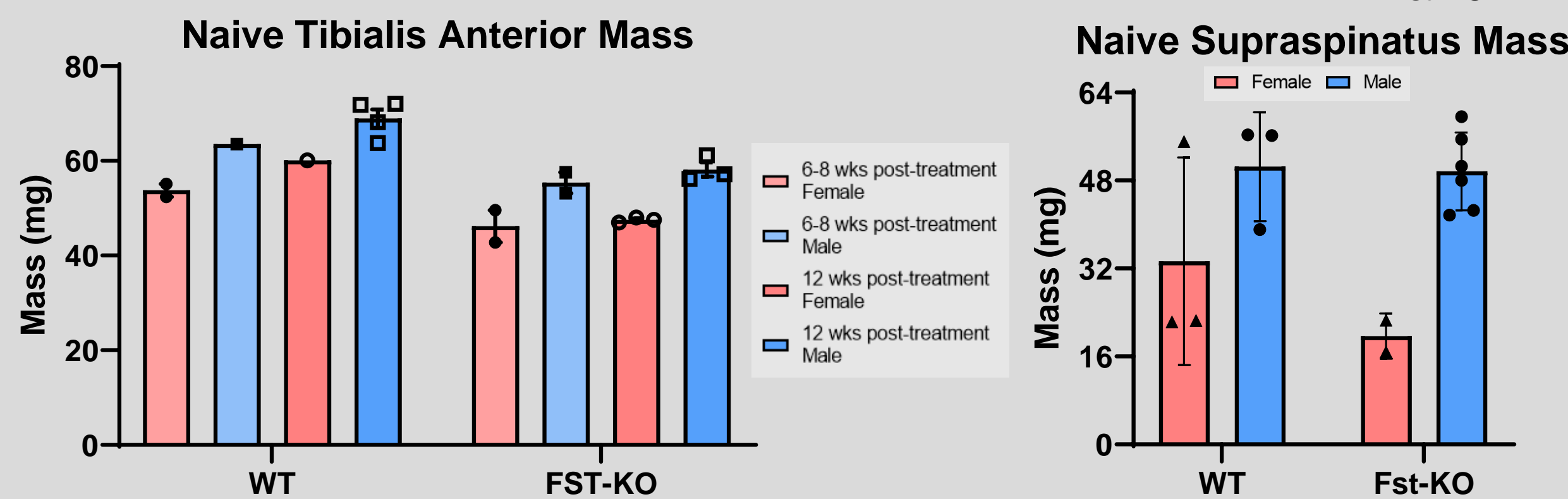


RESULTS

MASS DATA

Figure 6. TA masses after both contraction types were lower in FstKO mice. The masses of exercised TAs in the knockout mice were lower than those of the wild types. Sex was determined to be insignificant using a 2-way ANOVA.

Figure 7-8. No significant sex/genotype interaction in control supraspinatus Masses collected from unexercised muscles. Shows similar trend to Figure 5. Data in Figure 7 was collected from a previous cohort of mice. The supraspinatus masses were collected from the mice from this study.



FIBER TYPING

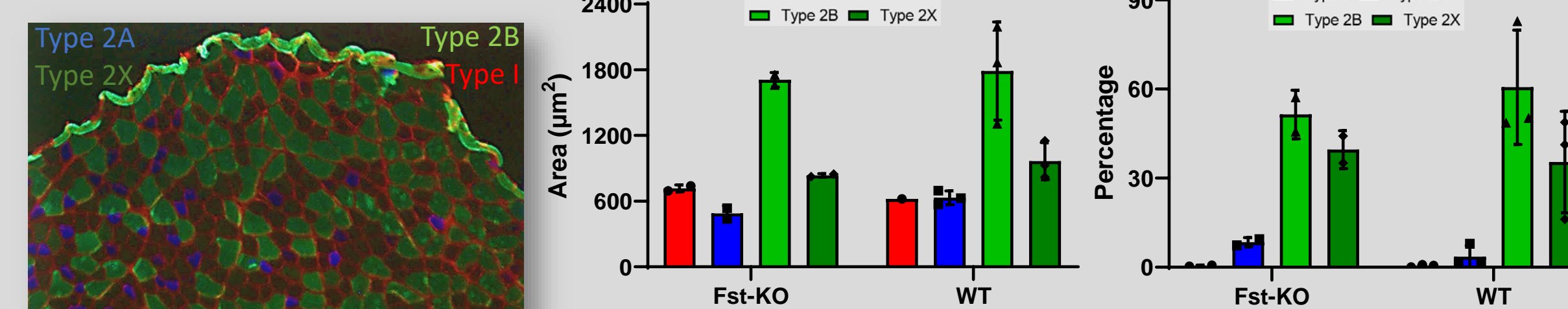
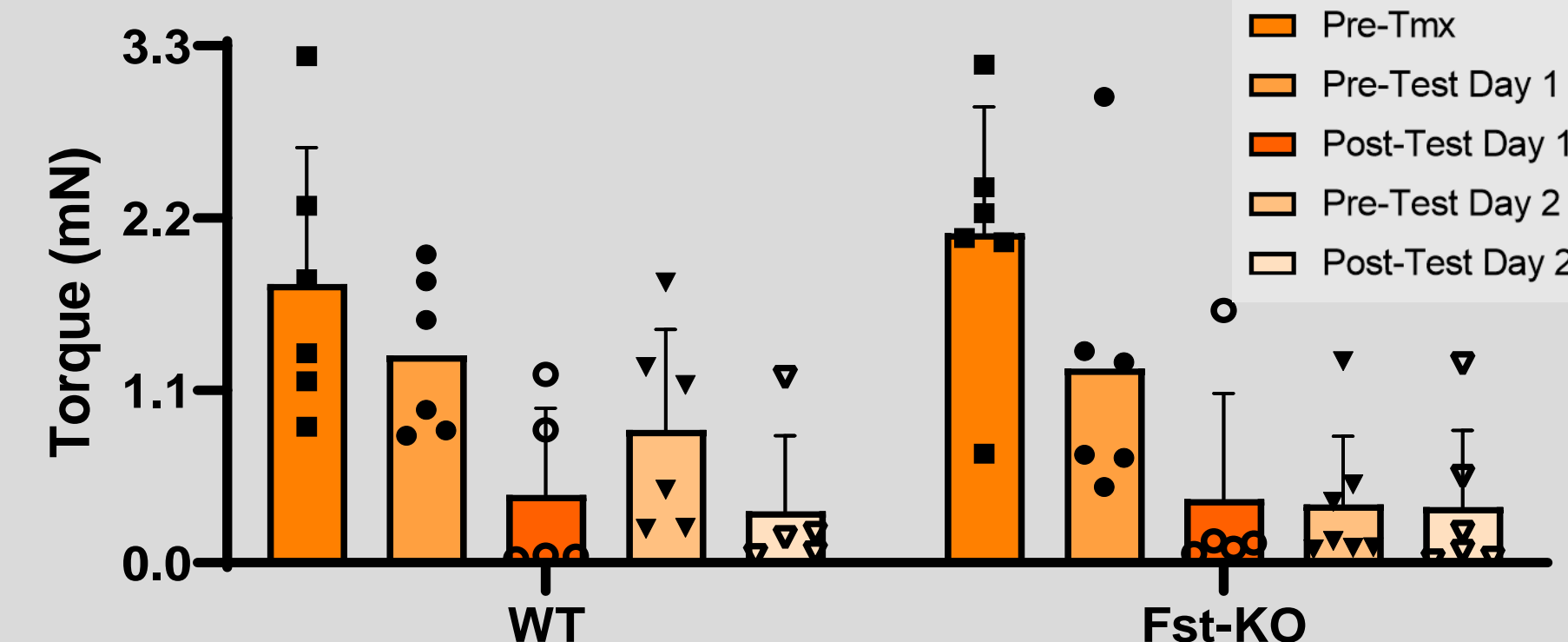


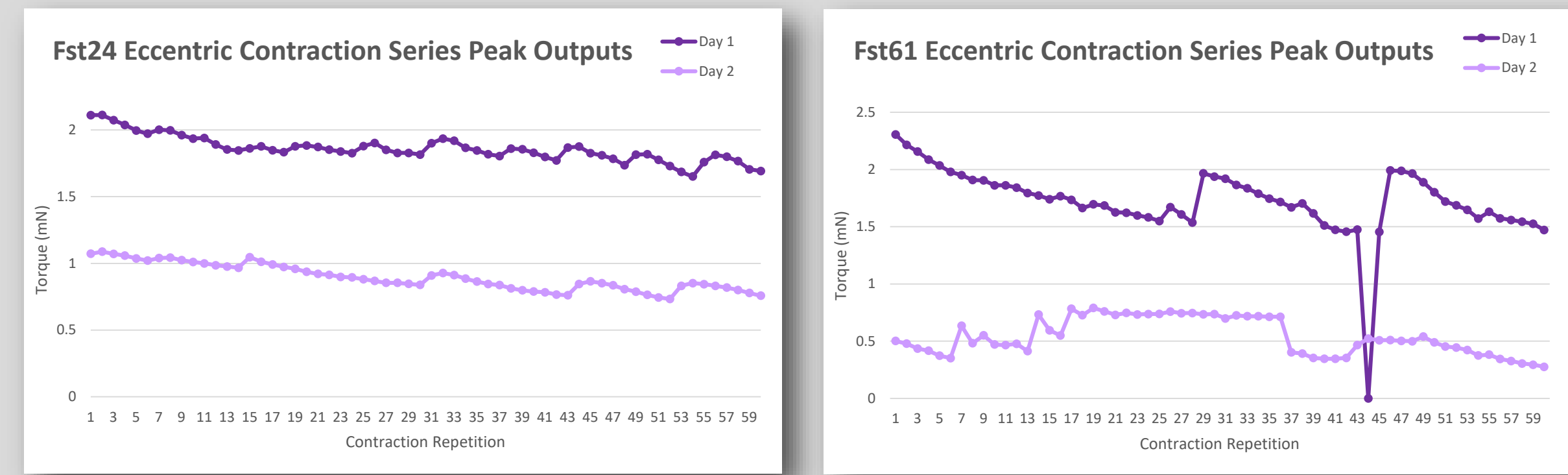
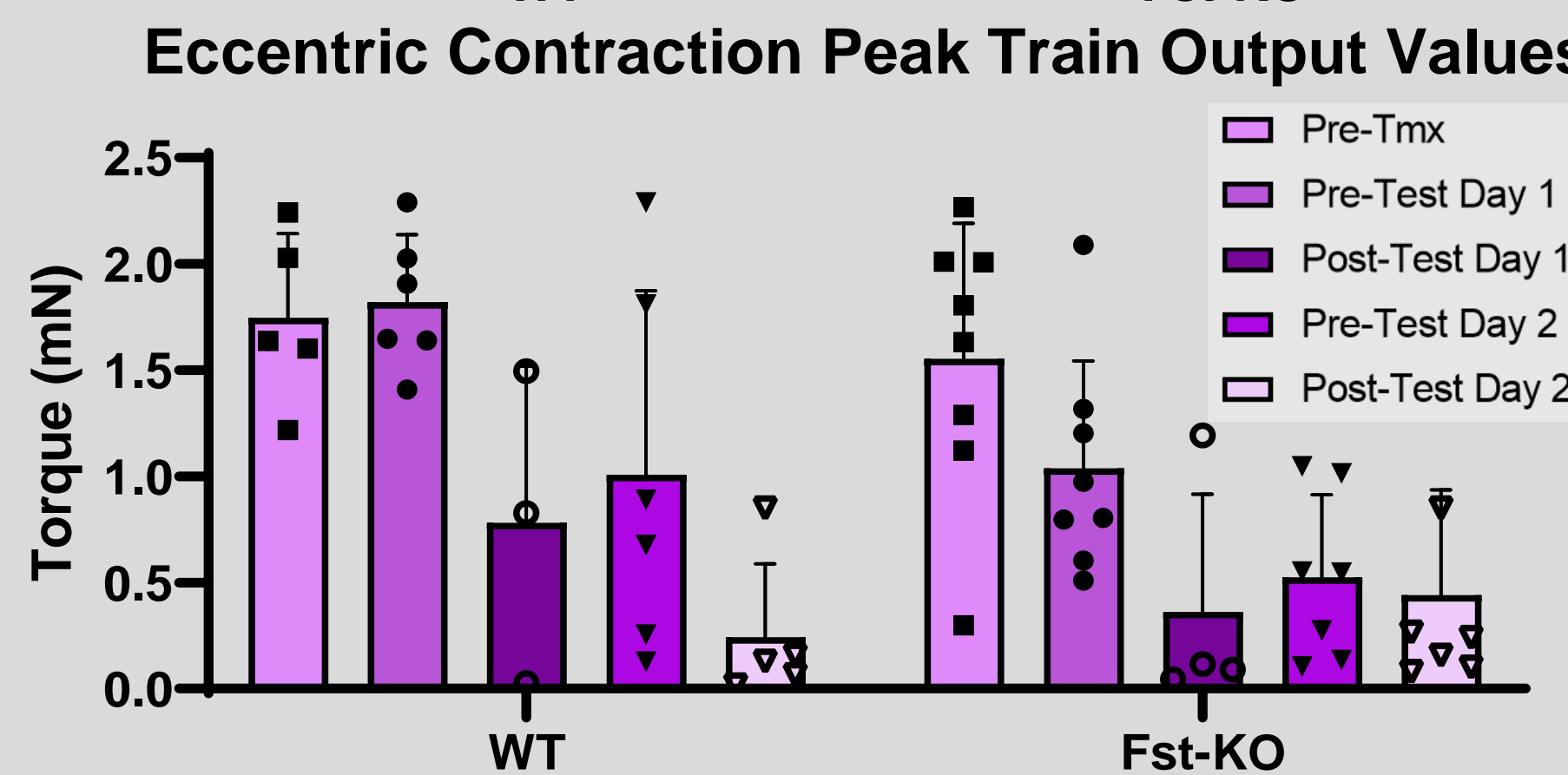
Figure 8-9. Composite Image & Data Quantification
There are less type 2B (fast twitch) fibers and more type 2A (intermediate) in the follistatin knockouts. Genotype is insignificant for average individual fiber area.

FORCE DATA

Figures 10-11. Peak Force Output Graphs
Outlier data was included because the variability could either be experimental or biological. Force recovery did occur with each contraction type for the Fst-KO mice.

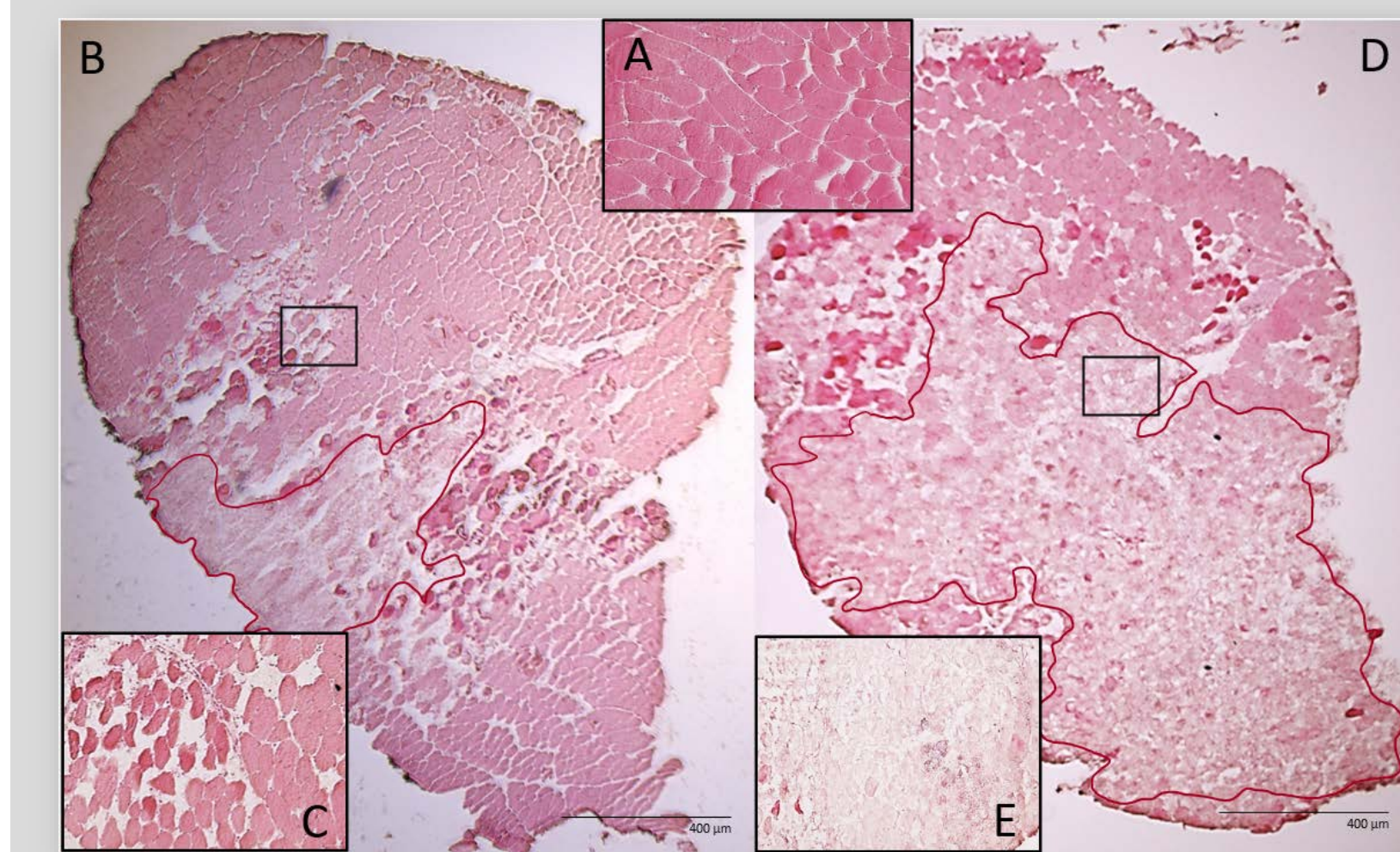


Figures 12-13 (below). Contrasting Examples of ECC Data
Image comparison demonstrates the extreme variability of force output throughout the protocol. The behavior in Figure 13 was expected as opposed to that in Figure 14. Proper needle placement was nearly impossible, making attaining consistent data massively difficult.



HISTOLOGY

Figure 15. H&E Staining & Necrosis Identification
(A) Healthy muscle fibers from a control supraspinatus section. (B) Full muscle section of an isometrically contracted TA. (C) 10x image of a region from the section in B with muscle fibers in varying stages of regeneration. (D) Eccentrically contracted TA. (E) 10x image of necrosis in D.



Percent Necrosis of Exercised TA Cross Sectional Area

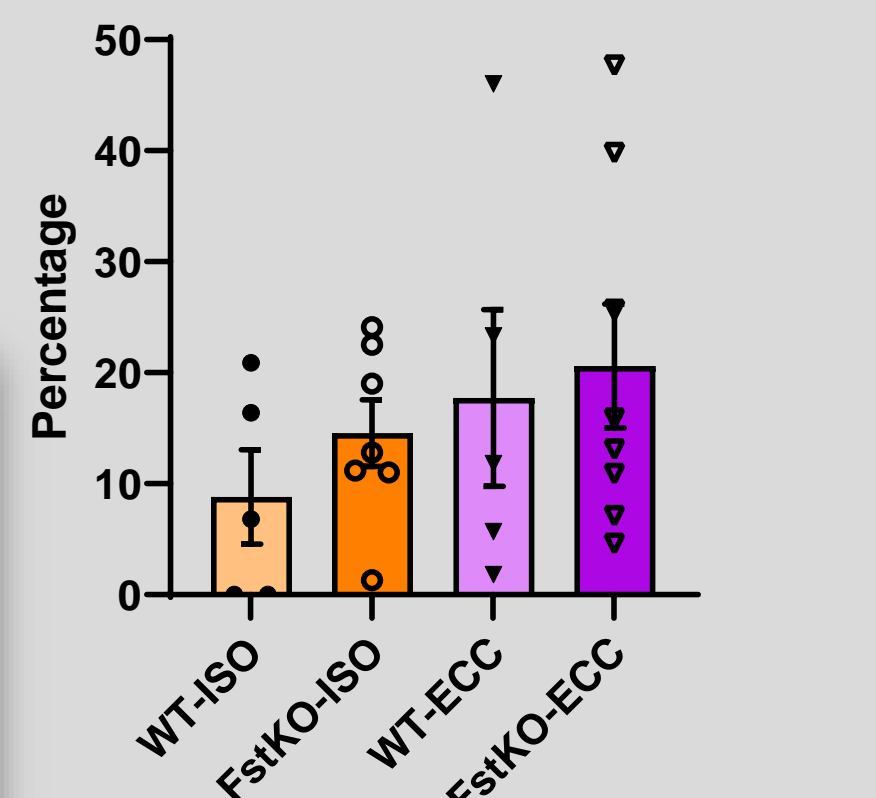


Figure 16. Degeneration Quantification
More necrosis (muscle death) occurred in ECC than ISO muscle. Degeneration is greater in FstKO mice than in WT.

WESTERN BLOTS

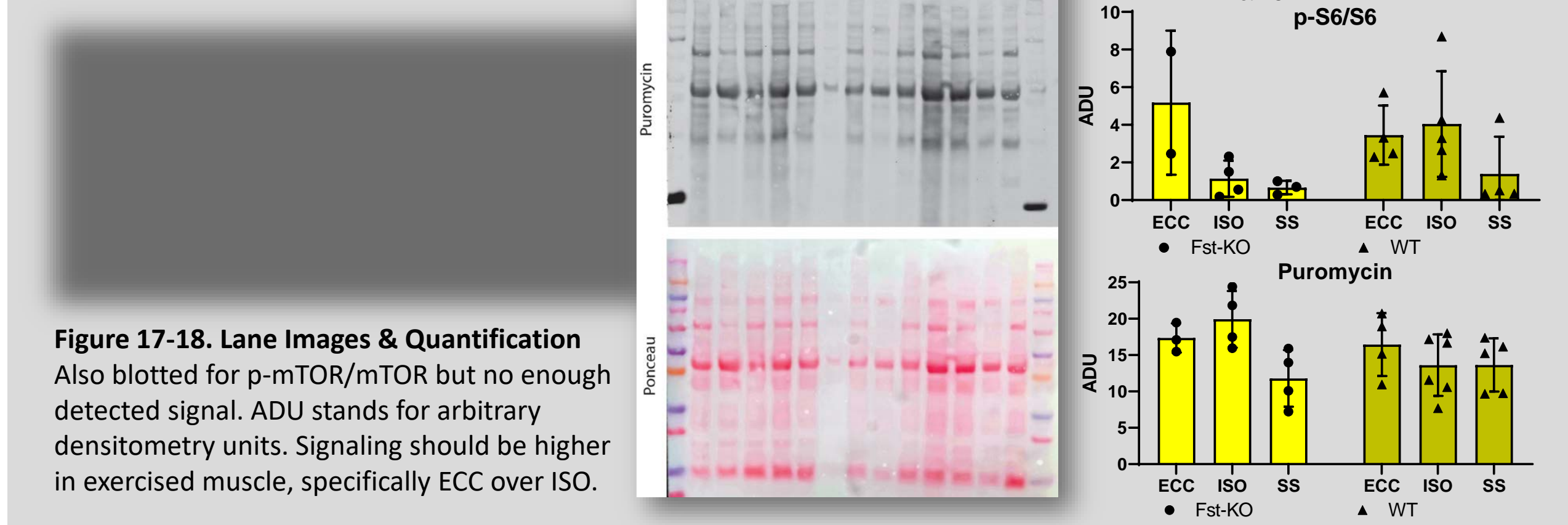


Figure 17-18. Lane Images & Quantification
Also blotted for p-mTOR/mTOR but no enough detected signal. ADU stands for arbitrary densitometry units. Signaling should be higher in exercised muscle, specifically ECC over ISO.

CONCLUSION

- Follistatin is required for mass maintenance
- Partial force recovery occurred so some muscle healing possible without Fst
- Study was underpowered to detect small differences between genotypes
- Unknown injury response shed light on the role of Fst in injury response
- Study provided insight into the signals that drive muscle recovery
- Potential connection between sarcopenia and follistatin deficiency
 - Sarcopenia: the muscle and strength loss that occurs in humans with age
 - Speculation that the condition could be partially attributed to a reduction in follistatin which circulates less with age
 - Mass data supported by mass & fiber type findings
- More focus on what might happen rather than how
- Limited ability to gather any information on long-term recovery
- Future work: reducing the damage done by the electrodes, considering a different injury model, and increasing the number of test subjects

ACKNOWLEDGEMENTS

I want to thank Karen Shen, Kay Bohnert, Jake Parson, and Dr. Gretchen Meyer of the Meyer Lab and Prof. Patricia Widder and Gwen Huyen from WashU & the CEMB for all of their help. Funding provided by the NSF through the CEMB.



References